Searching for QGP droplets with high-p_T hadrons and heavy flavor

Weiyao Ke* and Ivan Vitev†
Theoretical Division, Los Alamos National Laboratory, Los Alamos, New Mexico 87545, USA

(Received 22 April 2022; revised 17 March 2023; accepted 21 April 2023; published 5 June 2023)

The search for the smallest quark-gluon plasma (QGP) droplets in nature has motivated recent small collisions system programs at the BNL Relativistic Heavy Ion Collider (RHIC) and the CERN Large Hadron Collider (LHC). Unambiguous identification of jet quenching due to final-state interactions is key to confirming quark-gluon plasma (QGP) formation in these reactions. We compute the nuclear modification factors R_{AA} and $R_{p(d)A}$ of charged hadrons and heavy flavor mesons in large (Au-Au, Xe-Xe, Pb-Pb) and small (d-Au, p-Pb, O-O) colliding systems, respectively. Our results include the Cronin effect and initial-state parton energy loss in cold nuclear matter. In the final state, hard partons undergo collisional energy loss and branching that was recently derived using soft-collinear-effective-theory with Glauber gluons (SCET$_{\rm G}$). In large colliding systems, medium-modified quantum chromodynamics evolution of the fragmentation functions dominates the nuclear correction. As the system size decreases, we find that cold nuclear matter effects, collisional energy loss, and QGP-induced radiations can become equally important. A systematic scan over the medium size and mass or flavor dependence of R_{AA} provides the opportunity to separate these individual contributions and identify QGP signatures in small systems. Predictions for R^h_{AA}, R^D_{AA}, R^B_{AA} in O-O collisions at $\sqrt{s} = 0.2$ and 7 TeV are presented with and without the formation of a QGP and contrasted with the corresponding $R_{p(d)A}$ calculations. Single-hadron measurements at RHIC and the LHC will not only test the O-O predictions for both light and heavy flavor production but also shed light on the possibly very different dynamics of p-A and A-A reactions at similar soft particle production multiplicities.

DOI: 10.1103/PhysRevC.107.064903

I. INTRODUCTION

Jet quenching is an unambiguous signature of quark-gluon plasma (QGP) formation in nuclear collisions and has played a central role in its discovery at the BNL Relativistic Heavy Ion Collider (RHIC) [1–5]. Hard partons created in quantum chromodynamics (QCD) scattering processes undergo multiple collisions with the constituents in the hot QGP medium [6–16]. The interactions further amplify QCD radiation, which was first studied in the soft gluon emission limit [17–25]. The development of effective theories of QCD that describe parton interactions in matter via the exchange of Glauber gluons [26–29] has enabled calculations of full in-medium splitting functions [28,30,31]. As a result, medium-modified QCD evolution and parton shower calculations [32–34] have successfully explained the large factor of 5–10 suppression in the nuclear modification factor R_{AA} of hadron production in Au-Au and Pb-Pb collisions at the RHIC and the CERN Large Hadron Collider (LHC),

$$R_{AB} = \frac{dN_{AB\to h}(p_T)}{\langle T_{AB}\rangle d\sigma_{pp\to h}(p_T)}. \tag{1}$$

Here $\langle T_{AB}\rangle$ is the centrality-averaged geometric overlap function of nuclei with mass numbers A and B. Such success has also already motivated the reverse-engineering of the detailed transport parameters of jets in the QGP [35–39] and to use the internal structure of jets to understand the microscopic QGP properties [40–43].

Recently, puzzles have emerged in small colliding systems such as d-Au and p-Pb collisions. Similar "collective" behavior in the pattern of soft particle production that is attributed to QGP evolution in large systems has been observed [44–49], suggesting the possibility of final-state effects. However, clear evidence of jet quenching has not been established [50–55]. This puzzle has led to intense discussion of the origin of the apparent collectivity [56–59] and the nature of the medium produced in small systems. Sensitive experiments have been designed to provide further insight into this problem, such as the geometry scan at RHIC using p-Au, d-Au, and ^{3}He -Au [60–62], and the O-O collisions program at RHIC and LHC [63,64]. Theoretical predictions of jet quenching in O-O collisions already exist [65–68] for light and heavy-flavor quenching, using various frameworks, including transport equations and energy-loss calculations. In these studies, the QGP effects are modeled by medium-induced gluon radiation using either higher-twist [24] or the BDMPS-Z [17,18]

*weiyaoke@lanl.gov
†ivitev@lanl.gov

approach, and some studies also include collisional processes. Nevertheless, what is still missing from the theory side and the focus of this work is an analysis that combines QGP and full cold nuclear matter (CNM) effects to contrast results in $p(d)$-A and A-A reactions. This is an important step to establish the baseline without QGP formation and identify possibly different dynamics in symmetric versus asymmetric small systems. Then, we use in-medium QCD evolution formalism to consistently treat final-state parton shower effects for light and heavy flavor and understand the interplay with collisional energy loss.[1]

This paper aims to analyze the nuclear modification factors in various large and small systems. Calculations will be performed for light hadrons and heavy-flavor mesons, including both cold nuclear matter effects and hot QGP final-state effects, collisional energy loss and medium-induced radiation corrections to the baseline QCD factorization formalism. By fixing the jet-medium interaction parameter g_s in large colliding systems, we will make predictions for light and heavy-flavor productions in d-Au, p-Pb, O-O, with and without the assumption of the existence of a QGP.

The motivation for this comprehensive analysis is threefold. First, although initial-state cold nuclear matter effects are overwhelmed by the QGP-induced modifications in large systems, they can be important in small systems and provide an alternative explanation of the structure of modifications without resorting to the existence of a QGP. Second, the radiative correction can be strongly reduced relative to the collisional effect in a QGP of decreasing size, as we demonstrate in this paper. Therefore, a complete treatment of hot medium effects has to include elastic collisions. Using the distinct mass dependence of radiative and collisional processes, the difference between light and heavy flavor modifications in small systems can provide a handle on the relative contribution of the two. Third, a notable source of uncertainty that has hindered theoretical analyses in small systems is the decorrelation of charged particle production, which defines centrality classes, and the average nuclear overlap function $\langle T_{pA}\rangle$. The large model-dependence in T_{pA} complicates the interpretation of the present p-Pb modification data on hard probes. By looking into various collision geometries, especially light-ion collisions such as O-O, the normalization uncertainty is expected to be significantly reduced.

Finally, we remark that hadrons are ideal diagnostics of QGP quenching effects and have provided the definitive evidence for strong final-state interactions and the transverse momentum dependence of parton energy loss [70,71] at both RHIC and LHC. Azimuthal asymmetries at high p_T in A-A reactions are derivative signatures of jet quenching [72]. However, at small and intermediate transverse momenta in p-A and d-A, where we have data on hadron v_2, they may originate from cold nuclear matter effects [56,73]. Jet production and substructure is a new probe of parton shower modification in nuclear matter [74], but requires experimentally careful background subtraction. If strong suppression in the production rate of hard probes is unambiguously measured in small systems, jets could provide valuable complementary information on the QGP properties. For the purpose of first establishing jet quenching in p-Pb, d-Au, and small symmetric system like O-O, however, they offer no advantage over inclusive hadrons.

The rest of our paper is organized as follows: In Sec. II we review the factorization calculation in nuclear collisions and discuss the initial-state and final-state effects that will be considered. The dynamical approach to evaluating cold nuclear matter effects is described in Sec. III. In Sec. IV, we review in-medium QCD splitting functions obtained in $\mathrm{SCET_G}$, the modified QCD evolution for in-medium fragmentation function, and collisional energy loss in a thermal QGP. The model used to simulate the QGP medium is introduced in Sec. V. Results for R_{AA} in large and small systems are presented in Sec. VI. Finally, we give our conclusions in Sec. VII. The data-constrained parameters for hydrodynamic simulations are described in Appendix A. Light and heavy-flavor hadron production in proton-proton collisions and their scale dependence are discussed in Appendix B. We comment on the differences between dynamically calculated CNM effects and the parametrized nuclear parton distribution functions in Appendix C.

II. FACTORIZATION APPROACH WITH INITIAL AND FINAL-STATE EFFECTS

Calculations of hadron and jet production in reactions with nuclei are based on incorporating medium corrections into the perturbative QCD factorization approach. The baseline p-p transverse momentum (p_T) and rapidity (y) differential hadron production cross section is

$$\frac{d\sigma_h}{d\mathbf{p}^2 dy} = \sum_k \int_0^1 \frac{dz}{z^2} D_{h/k}(z;\mu_F) \frac{d\sigma_k}{d\mathbf{q}^2 dy}\left(\frac{\mathbf{p}}{z};\mu_F,\mu_R\right). \quad (2)$$

$D_{h/k}(z,\mu_F)$ is the fragmentation function of parton k into hadron h carrying momentum fraction z. Final-state effects in the QGP modify $D_{h/k}(z,\mu_F)$, and the fragmentation will generally depend on the parton energy E in the rest frame of the medium in addition to the medium transport properties β,

$$D_{h/k}(z;\mu_F) \to D_{h/k}(z;\mu_F;E,\beta). \quad (3)$$

$d\sigma_k/dq_T^2 dy$ is the production cross section of the hard parton and accounts for many-body scattering effects in large nuclei. It can be expressed as

$$\frac{d\sigma_k}{d\mathbf{q}^2 dy} = \frac{4}{s}\sum_{ij}\int d\eta_{\mathrm{c.m.}} \int d^2\mathbf{k}_i f_{i/A}(x_i+\Delta x_i,\mathbf{k}_i;\mu_F) \times \int d^2\mathbf{k}_j f_{j/B}(x_j+\Delta x_j,\mathbf{k}_j;\mu_F) \times \frac{d\sigma_{ij\to k}}{d\cos\theta_{\mathrm{c.m.}}}(x_i x_j s,\cos\theta_{\mathrm{c.m.}};\mu_R). \quad (4)$$

Here, $\sigma_{ij\to k}$ is the perturbative partonic cross section. The integration has been transformed to the pseudorapidity ($\eta_{\mathrm{c.m.}}$) of the produced particle in the partonic center-of-mass frame,

[1]Medium-modified Dokshitzer-Gribov-Lipatov-Altarelli-Parisi (DGLAP) evolution has also been applied to understand the suppression of hadrons at the future Electron-Ion Collider [69].

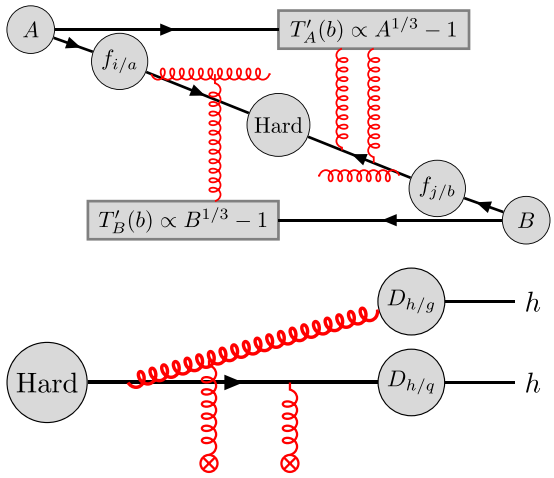

FIG. 1. (upper panel) Illustration of cold nuclear matter effects. Vertical gluon lines represent multiple collisions between initial-state partons with the other nucleus. Horizontal lines represent the modified gluon radiation in the initial state. (lower panel) Illustration of final-state effects of jets in the quark-gluon plasma.

and $\cos\theta_{\rm c.m.} = \tanh\eta_{\rm c.m.}$ is the polar angle. We will set the factorization and renormalization scale to the transverse momentum of the hard parton $\mu_R = \mu_F = |\mathbf{q}| = |\mathbf{p}|/z$.

Equation (4) accounts for the fact that initial partons can acquire a finite transverse momentum $\mathbf{k}_i$, $\mathbf{k}_j$ from multiple collisions with the other nucleus, which we treat in the Gaussian approximation [20,75] that is often used to describe the Cronin effect [76]. x_i and x_j are the longitudinal momentum fractions that can be found from

$$y = \frac{1}{2}\ln\frac{x_i}{x_j} + \eta_{\rm c.m.}, \tag{5}$$

$$\left[\mathbf{q} - \frac{\mathbf{k}_i + \mathbf{k}_j}{2}\right]^2 = \frac{x_i x_j s \sin^2\theta_{\rm c.m.}}{4}. \tag{6}$$

Another impact of cold nuclear matter is that initial-state partons can lose fractions ($\Delta x_i/x_i$ and $\Delta x_j/x_j$) of their energy due to CNM-induced gluon emissions [77]. The physical pictures behind equations (4) and (2) are illustrated in the upper and lower panel of Fig. 1. Finally, coherent scatterings also lead to the dynamical shadowing effect that further shifts the x_i by an amount proportional to the nuclear thickness function [78]. It only contributes at small Bjorken x and low transverse momentum and we do not write it explicitly in equation (4). We will elaborate upon these CNM effects in Sec. III.

III. THE DYNAMICAL APPROACH FOR COLD NUCLEAR MATTER EFFECTS

Despite the complicated nature of parton interaction in the nuclear environment, it is possible to model the initial-state effect from QCD interactions. In Ref. [77], one considers multiple scattering (vertical gluons lines in the upper panel of Fig. 1) and induced soft gluon radiation (horizontal gluons lines in the upper panel of Fig. 1) from initial-state partons as they traverse in the nuclear matter before the hard interaction. Collisions shift particle spectra to slightly larger transverse momentum, resulting in an enhancement at p_T around a few GeV, known as the Cronin effect [76]. The interaction potential between partons and the cold nuclear matter (CNM) is modeled by a screened Coulomb potential with typical transverse momentum transfer squared $\mu^2 = 0.12$ GeV^2 and mean-free paths $\lambda_g = (C_F/C_A)\lambda_q = 1.5$ fm. As mentioned earlier, we employ the Gaussian parametrization of the Cronin effect and account for the power-law tails of the Moliere multiple scattering with a numerical factor $\xi \approx$ few. The magnitude of the Cronin effect is sensitive to the shape of the particle spectra and decreases at large colliding energies [79]. For phenomenological applications we also consider 50% shorter mean-free paths to estimate its uncertainty.

At small transverse momenta and small values of Bjorken-x coherent multiple scattering also leads to dynamical shadowing [78,80], which we include in the calculation as a shift in the x variables. Coherent power corrections scale as $\delta x_i/x_i \sim \mu^2 A^{1/3}/(-u)$ and $\delta x_j/x_j \sim \mu^2 B^{1/3}/(-t)$ in A-B reactions and t and u are the partonic Mandelstam variables for the hard scattering process.

The Cronin and dynamical shadowing effects disappear at high p_T. On the contrary, induced gluon emissions that cause initial-state parton energy loss in CNM continue to be important at high energy [77,81]:

$$x\frac{dN_{\rm IS}}{dxd^2\mathbf{k}} = \frac{\alpha_s C_R}{\pi^2}\frac{L}{\lambda_g}\int_0^{\frac{\mu p^+}{4}} d^2\mathbf{q}\frac{\mu^2}{\pi(\mathbf{q}^2+\mu^2)^2} \times\left[\frac{\mathbf{q}^2}{\mathbf{k}^2(\mathbf{k}-\mathbf{q})^2} - \frac{2(\mathbf{q}^2 - \mathbf{q}\cdot\mathbf{k})}{\mathbf{k}^2(\mathbf{k}-\mathbf{q})^2}\frac{\sin\frac{\mathbf{k}^2 L}{xp^+}}{\frac{\mathbf{k}^2 L}{xp^+}}\right]. \tag{7}$$

Here, x is the momentum fraction carried away by the radiated gluon. L is the path length that parton propagates in the cold nuclear matter before the hard collision. The same transverse-momentum transfer squared μ^2 and mean-free path λ_g are used in equation (7) as those for the Cronin effect. The CNM energy loss also causes a shift in the momentum fraction x of the initial parton in equation (4):

$$\frac{\Delta x}{x} = \epsilon_{\rm fl}\int_{m_N/p^+}^1 dx\int_{xm_N\leqslant|\mathbf{k}|\leqslant xp^+} d^2\mathbf{k}x\frac{dN_{\rm IS}}{dxd^2\mathbf{k}}, \tag{8}$$

with m_N the mass of the nucleon. At high energy, the CNM energy-loss contribution is approximately linearly proportional to L [79]. Therefore, for each collision centrality an averaged path length obtained from the TRENTo model's [82] simulation of the collision geometry have been used in equations (7) and (8). This introduces the centrality dependence of CNM effects, while path-length fluctuations at a given impact parameter are neglected. Furthermore, fluctuations due to multiple gluon emissions effectively reduce the mean fractional energy loss, which we account for with $\epsilon_{\rm fl} < 1$. For steeply falling final-state spectra $\epsilon_{\rm fl}$ can be as small as 0.4 [83]. The energy dependence of the initial parton flux is much more moderate and we use $\epsilon_{\rm fl} = 0.7$. For phenomenological applications, we also consider the scenario without initial-state energy loss.

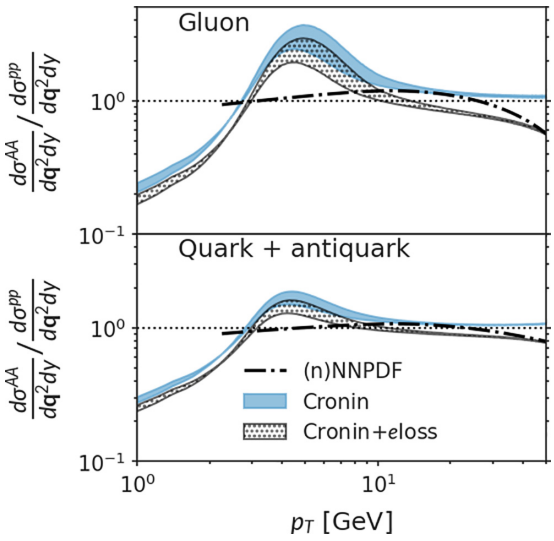

FIG. 2. Comparison of cold nuclear matter effects in Au-Au collisions at $\sqrt{s} = 200$ GeV from (I) (n)NNPDF (black lines); (II) dynamical approach without CNM energy loss (blue bands), where bands indicate the variation of the strength of Cronin effect; and (III) dynamical approach with CNM energy loss (dotted bands).

The calculation that includes the Cronin effect, dynamical shadowing, and the CNM energy loss, hereafter referred to as the "dynamical CNM calculation" or "Cronin + *e*loss," will be used as the primary model for how the nuclear environment affects the initial parton density $f(x, \mathbf{k})$. The advantage of the dynamical approach is that one can use only two parameters that control the magnitude of broadening and initial-state energy loss to systematically study the energy and A dependence predicted by QCD. In the large-x region, the current calculation only implements the isospin effect without parametrizing the antishadowing, EMC, and Fermi motion regions. We expect these effects to be small for the moderate-p_T regions of hadron production considered in this paper.

By carefully selecting the colliding system, the measured final-state, the center-of-mass energy, and the kinematic region, we can enhance the sensitivity to individual CNM effects. In heavy ion collisions, however, they all can play a role in modifying the hadron and jet cross sections. To illustrate this, in Fig. 2 we compute the spectra of partons produced in the hard interaction in Au-Au collisions relative to the scaled p-p baseline at $\sqrt{s} = 200$ GeV. The blue bands are dynamical model calculations with Cronin and dynamical shadowing effects only, and shaded bands are results that further include the CNM energy loss. The spread of the bands represents 50% variation in the magnitude of transverse momentum broadening. Scattering in nuclear matter introduces a nuclear size-dependent enhancement at moderate p_T, while depleting particle production below 2 GeV. Dynamical shadowing also contributes to this low-p_T suppression [78]. The CNM energy loss suppresses the spectra at large p_T. The dynamical CNM calculations are compared with results using collinear nuclear parton distribution functions (nPDFs) from the (n)NNPDF Collaboration [84] (black dash-dotted lines). There is no momentum broadening in the collinear nPDF. The small low-p_T suppression comes from the parametrized shadowing effect. At large p_T, modifications results from the antishadowing, EMC, and the Fermi motion effects included in the nPDF. Unlike the dynamical CNM model, nNNPDF does not depend on the impact parameter, which is essential to include to study the centrality dependence of R_{AA} and R_{pA} in small colliding systems. Therefore, we primarily use the dynamical CNM model in this paper and will compare the impact of using nPDF to the final results in Appendix C.

IV. FINAL-STATE QUARK GLUON PLASMA EFFECTS

A. Medium-modified splitting functions in SCET$_G$

An effective theory of QCD ideally suited to studying jet physics is the soft-collinear-effective-theory (SCET) [85,86]. The power counting parameter $\lambda = |\mathbf{k}|/p^+$ can be thought of as the typical transverse momentum in the jet divided by its large light-cone component. In reactions with nuclei, the SCET$_G$ theory [26,27] was developed to couple the collinear fields to the background nuclear medium via Glauber gluon exchanges. Thus, hadron and jet production, and jet substructure can be described in different strongly interacting environments without loss of generality. This framework has been applied to study both the jet broadening [87] and derive the medium-modified QCD splitting functions [30,88].

For phenomenological application, the Glauber gluon field is often approximated by a sum of static-screened color potentials over the scattering centers in the medium

$$V_R^a(\mathbf{q}) = \sum_i g_s^2 \frac{T^a(R) \otimes T^a(i)}{\mathbf{q}^2 + m_D^2} e^{-i\mathbf{q}\cdot\mathbf{z} - i\frac{1}{2}q^- z^+}. \tag{9}$$

Here, R denotes the color representation of the collinear parton while i is the representation of the color charge of the medium quasiparticle. g_s is the jet-medium coupling constant. $m_D^2 = g_s^2(1 + \frac{N_f}{6})T^2$ is the Debye screening mass in the plasma. There is no momentum exchange in the p^+ direction that scales stronger than λ^2.

The phase factor contains the position $(\mathbf{z}, z^+)$ information of the medium color charge.[2] The differential collision rate between a collinear quark (or gluon) and the QGP is

$$\frac{dR_{q,g}(x)}{d^2\mathbf{q}} = \frac{\lambda_{q,g}^{-1}}{\pi} \frac{m_D^2}{\left(\mathbf{q}^2 + m_D^2\right)^2}, \tag{10}$$

with $\lambda_g^{-1} = \frac{C_A}{C_F}\lambda_q^{-1} = \frac{\zeta(3)T^3}{\pi^2}(2d_A + \frac{C_F}{C_A}3d_F N_f)\sigma_{gg}$ being the inverse mean-free-path of the parton in the plasma and $\sigma_{gg} = (9/32\pi)(g_s^4/m_D^2)$ is the screened Coulomb cross-section of gluons. $\zeta(3) \approx 1.2$, $d_A = N_c^2 - 1$, $d_F = N_c$, and we choose an effective $N_f = 2$ for the QGP.

The modified QCD splitting functions have been obtained to the first order in opacity explicitly [27,30] and an iterative approach has been developed to generalize them to higher opacity orders [89]. For light partons, we take the full splitting function to first order, which we quote for completeness from

[2]We use the convention $x^\pm = x^0 \pm x^3$.

Ref. [30]. The double-differential spectrum of the quark to quark + gluon branching is

$$\frac{dN_{qq}^{\rm med}}{dxd\mathbf{k}^2} \equiv P_{qq}(x,\mathbf{k}^2)\int_0^\infty d\Delta z\int d^2\mathbf{q}\frac{dR_g(\Delta z)}{d^2\mathbf{q}}\left\{\left[\frac{\mathbf{B}}{\mathbf{B}^2}\cdot\left(\frac{\mathbf{B}}{\mathbf{B}^2}-\frac{\mathbf{C}}{\mathbf{C}^2}\right)+\frac{1}{N_c^2}\frac{\mathbf{B}}{\mathbf{B}^2}\cdot\left(\frac{\mathbf{A}}{\mathbf{A}^2}-\frac{\mathbf{B}}{\mathbf{B}^2}\right)\right][1-\cos(\omega_1\Delta z)]\right.$$
$$+\frac{\mathbf{C}}{\mathbf{C}^2}\cdot\left(2\frac{\mathbf{C}}{\mathbf{C}^2}-\frac{\mathbf{A}}{\mathbf{A}^2}-\frac{\mathbf{B}}{\mathbf{B}^2}\right)[1-\cos(\omega_2\Delta z)]+\frac{\mathbf{B}}{\mathbf{B}^2}\cdot\frac{\mathbf{C}}{\mathbf{C}^2}[1-\cos(\omega_3\Delta z)]$$
$$\left.-\frac{\mathbf{A}}{\mathbf{A}^2}\cdot\left(\frac{\mathbf{A}}{\mathbf{A}^2}-\frac{\mathbf{D}}{\mathbf{D}^2}\right)[1-\cos(\omega_4\Delta z)]-\frac{\mathbf{A}}{\mathbf{A}^2}\cdot\frac{\mathbf{D}}{\mathbf{D}^2}[1-\cos(\omega_5\Delta z)]\right\}, \tag{11}$$

where the gluon carries momentum fraction x. Note that this differs from the standard high-energy notation and is done to make contact with the much studies energy loss soft gluon emission limit when $x\to 0$. The quark to gluon + quark splitting function is obtained by $dN_{gq}^{\rm med}/dxd\mathbf{k}^2(x) = dN_{qq}^{\rm med}/dxd\mathbf{k}^2(1-x)$. For gluon to quark + quark and gluon to gluon + gluon splittings, the distributions are

$$\frac{dN_{\{gg,qg\}}^{\rm med}}{dxd\mathbf{k}^2} \equiv P_{\{gg,qg\}}(x,\mathbf{k}^2)\int_0^\infty d\Delta z\int d^2\mathbf{q}\frac{dR_{\{g,q\}}(\Delta z)}{d^2\mathbf{q}}\left\{2\left[\frac{\mathbf{B}}{\mathbf{B}^2}\cdot\left(\frac{\mathbf{B}}{\mathbf{B}^2}-\frac{\mathbf{A}}{\mathbf{A}^2}\right)+\left\{-\frac{1}{2},\frac{1}{d_A}\right\}\frac{\mathbf{B}}{\mathbf{B}^2}\cdot\left(\frac{\mathbf{C}}{\mathbf{C}^2}-\frac{\mathbf{A}}{\mathbf{A}^2}\right)\right][1-\cos(\omega_1\Delta z)]\right.$$
$$+2\frac{\mathbf{C}}{\mathbf{C}^2}\cdot\left(\frac{\mathbf{C}}{\mathbf{C}^2}+\frac{\mathbf{B}}{\mathbf{B}^2}-2\frac{\mathbf{A}}{\mathbf{A}^2}\right)[1-\cos(\omega_2\Delta z)]-2\frac{\mathbf{B}}{\mathbf{B}^2}\cdot\frac{\mathbf{C}}{\mathbf{C}^2}[1-\cos(\omega_3\Delta z)]$$
$$\left.+2\frac{\mathbf{A}}{\mathbf{A}^2}\cdot\left(\frac{\mathbf{A}}{\mathbf{A}^2}-\frac{\mathbf{D}}{\mathbf{D}^2}\right)[1-\cos(\omega_4\Delta z)]+2\frac{\mathbf{A}}{\mathbf{A}^2}\cdot\frac{\mathbf{D}}{\mathbf{D}^2}[1-\cos(\omega_5\Delta z]\right\}. \tag{12}$$

In the above expressions, we have defined vectors

$$\mathbf{A}=\mathbf{k},\quad \mathbf{B}=\mathbf{k}+x\mathbf{q},$$
$$\mathbf{C}=\mathbf{k}-(1-x)\mathbf{q},\quad \mathbf{D}=\mathbf{k}-\mathbf{q}, \tag{13}$$

and frequencies (which are inverse formation times)

$$\omega_1=\frac{\mathbf{B}^2}{x(1-x)p^+},\quad \omega_2=\frac{\mathbf{C}^2}{x(1-x)p^+},$$
$$\omega_3=\frac{\mathbf{C}^2-\mathbf{B}^2}{x(1-x)p^+},\quad \omega_4=\frac{\mathbf{A}^2}{x(1-x)p^+}, \tag{14}$$
$$\omega_5=\frac{\mathbf{A}^2-\mathbf{D}^2}{x(1-x)p^+}.$$

In the medium, partons acquire effective mass that we implement as $\mathbf{V}^2\to\mathbf{V}^2+m_D^2$ with $\mathbf{V}$ being any of the $\mathbf{A},\mathbf{B},\mathbf{C},\mathbf{D}$ vectors in the propagators and frequencies ω_i. Since the thermal mass m_D is larger than the nonperturbative cutoff $k_{T,\rm min}$, the running of α_s associated with the medium-induced splitting vertex are effectively screened by m_D^2 at very small virtualities.

P_{qq}, P_{gq}, P_{gg}, P_{qg} are the standard splitting functions in the vacuum at leading order:

$$P_{qq}=\frac{\alpha_s}{2\pi}C_F\frac{1+(1-x)^2}{x}, \tag{15}$$
$$P_{gg}=\frac{\alpha_s}{2\pi}C_A\frac{1+x^4+(1-x)^4}{x(1-x)}, \tag{16}$$
$$P_{gq}=\frac{\alpha_s}{2\pi}C_F\frac{1+x^2}{1-x}, \tag{17}$$
$$P_{qg}=\frac{\alpha_s}{2\pi}T_F[x^2+(1-x)^2]. \tag{18}$$

The coupling constants α_s associated with the vacuum splitting vertices in the medium-induced splitting functions are evaluated at scale $\mathbf{k}^2$ in this study, while the jet-medium coupling parameter g_s that goes into the collisions rates $dR/d\mathbf{q}^2$ is taken as a free parameter. The $\mathbf{q}$ integration is restricted by $\mathbf{k}^2 < p^+\mu_D/2$. Equations (11) and (12) are the medium corrections to the real emission function of the splitting. In Sec. IV D, we discuss the inclusion of both real emission and virtual corrections in the DGLAP evolution equation.

Equations (11) and (12) give the medium-induced branching kernels along a give path $\mathbf{x}+\hat{\phi}\Delta z$ of the jet parton in the medium. $\mathbf{x}$ and $\hat{n}$ are the initial transverse location of the hard production vertex and a unit vector pointing in the direction of parton propagation. The collision rates $dR_{\{g,q\}}/d^2\mathbf{q}$ are then obtained along the quark or gluon trajectory. In practical simulations these expressions are embedded and averaged in a dynamical medium with the space-time temperature profile of the QGP obtained in a 2 + 1D hydrodynamic simulation (see Sec. V). The medium-averaged splitting functions are given by

$$\left\langle\frac{dN^{\rm med}}{dxd\mathbf{k}^2}\right\rangle \equiv \int_0^{2\pi}\frac{d\phi}{2\pi}\int d^2\mathbf{x}\frac{dP_{\rm coll}}{d^2\mathbf{x}}\frac{dN^{\rm med}}{dxd\mathbf{k}^2}(\mathbf{x}). \tag{19}$$

$dP_{\rm coll}/d^2\mathbf{x}$ is the normalized density of binary collision in a plane transverse to the collision axis for a given centrality obtained from the TRENTo initial condition model. Hereafter, all splitting functions we use include this medium-averaging, but we omit writing the brackets $\langle\cdots\rangle$ for brevity. In performing the above integration, a constant QGP formation time $\tau_0 = 0.6$ fm is used for all systems, after which hard partons start to interact with the medium. The interaction is eventually switched off at temperature $T = 160$ MeV.

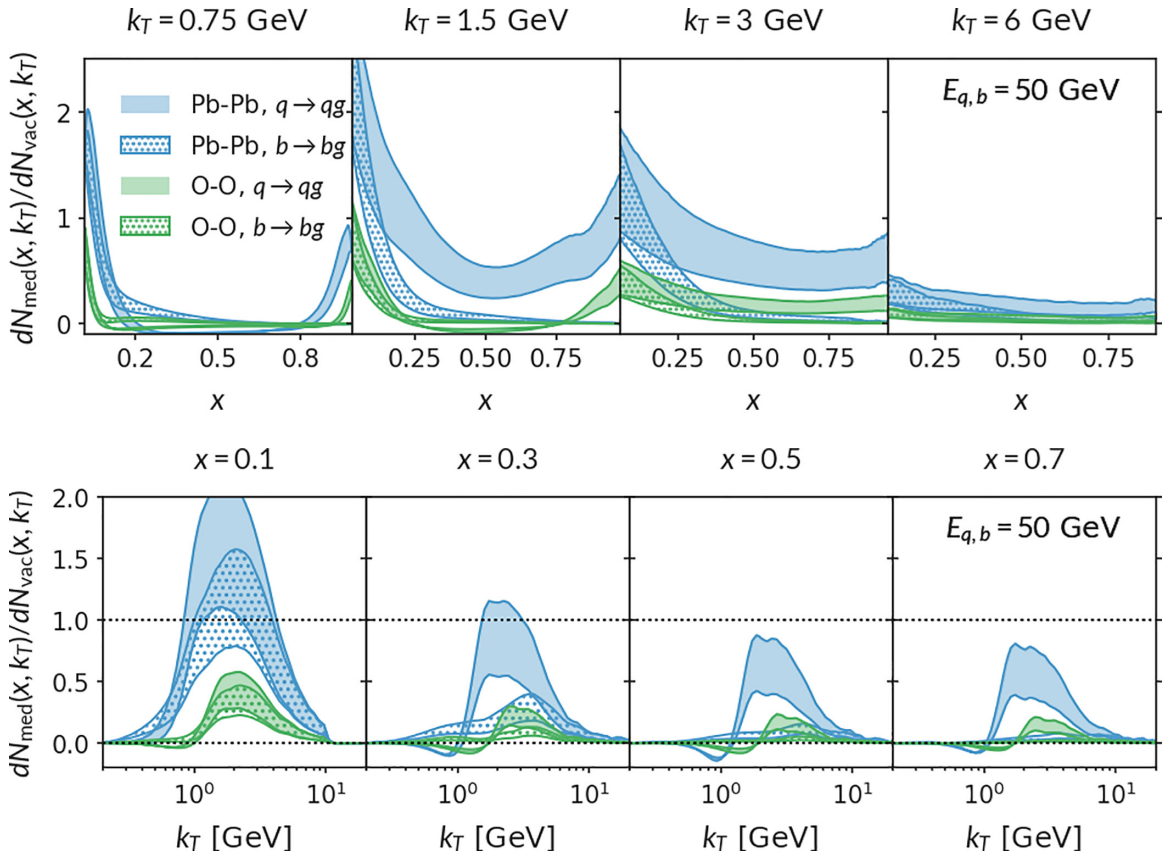

FIG. 3. The medium-induced contribution to the QCD splitting function $dN_{\rm med}/dxd^2\mathbf{k}$ divided by $dN_{\rm vac}/dxd^2\mathbf{k}$ for the $q \to q + g$ (filled bands) and $b \to b + g$ (dotted bands) channels. (upper panel) The corrections are shown as a function of gluon momentum fraction x at four different k_T. The bands show the variation of the correction within $1.6 < g_s < 2.0$. Blue and green colors label the results for central Pb-Pb collisions at 5.02 TeV and central O-O collisions at 7 TeV, respectively. (lower panel) Same as above, but with modifications shown as functions of k_T. Note that in a hot QGP medium, the contribution at very small k_T is highly suppressed.

The vacuum splitting functions involving heavy quarks H ($H = c, b$) with mass M are

$$P_{HH} = \frac{\alpha_s}{2\pi} C_F \left[\frac{1 + (1-x)^2}{x} - \frac{2x(1-x)M^2}{\mathbf{k}^2 + x^2M^2} \right], \quad (20)$$

$$P_{gH} = \frac{\alpha_s}{2\pi} C_F \left[\frac{1 + x^2}{1-x} - \frac{2x(1-x)M^2}{\mathbf{k}^2 + (1-x)^2M^2} \right], \quad (21)$$

$$P_{Hg} = \frac{\alpha_s}{2\pi} T_F \left[x^2 + (1-x)^2 + \frac{2x(1-x)M^2}{\mathbf{k}^2 + M^2} \right]. \quad (22)$$

The x dependence can be significantly modified compared with light flavors when $\mathbf{k}^2 \lesssim M^2$. The formulas for the medium corrections to equations (20)–(22) have been derived in Ref. [28]. Although we will not write down the full in-medium expressions, we emphasize that the heavy quark mass not only introduces corrections to the propagators and the interference phases but also generates many new terms proportional to the squared quark mass.

We demonstrate the impact of mass corrections in the medium with numerical results, as shown in Fig. 3. The medium-correction to $q \to q + g$ and $b \to b + g$ splitting functions in 0%–5% central Pb-Pb collisions at 5.02 TeV and in 0%–5% O-O at 7 TeV are presented. We have factored out the vacuum-like P_{qq} and P_{bb} kernels given by equation (18) and equation (20). For the bottom quark, the vacuum splitting functions P_{bb} shows the so-called dead-cone effect that suppress radiations in the phase-space region $x > |\mathbf{k}|/M$ relative to P_{qq}. However, after factoring out the vacuum factor, the ratio still displays strong mass modifications [43]. Only ratios in the energy-loss region $x \to 0$ are comparable to that of the light quark.

The $|\mathbf{k}|$-dependence calculated within $k_{T,\rm min} = 0.2$ GeV $< \mathbf{k} < xp^+$ is shown in the lower panel of Fig. 3. Medium-induced branchings are suppressed at large $\mathbf{k}$ by at least another power of $1/\mathbf{k}^2$ as compared with the vacuum radiation. Meanwhile, the LPM interference factors in equations (11) and (12) suppress collinear splittings with $\omega_i \lesssim \Delta z$. As a result, medium-modified contributions acquires a typical transverse momentum that peaks above 1 GeV in this case, which makes the perturbative calculation of hadron quenching more reliable. The typical $\mathbf{k}$ is larger for the case of heavy quarks and for calculations in small systems as the typical Δz is smaller. In central Pb-Pb collisions, the correction at its peak can be much larger than the vacuum contribution. In central O-O collisions at 7 TeV, it is estimated to be about

a factor of three smaller than in central Pb-Pb at 5 TeV, assuming QGP effects do exist in O-O.

B. Collisional energy loss

In obtaining equations (11) and (12), one assumes that p^+ is conserved. This is a good approximation for the computation of radiative correction because a mismatch in p^+ due to collisional energy losses is expected to be subleading in powers of λ [89]. However, collisional energy loss should be taken into account to compute R_{AA} at intermediate and small p_T [10,15,90]. It was found that it can be comparable to the radiative energy loss for partons up to $p_T = 10$ to 20 GeV. For heavy flavor particles, due to the reduced phase space for radiation when p_T is only a few times the heavy quark mass M and the dead cone effect, collisional energy loss is even more important to describe heavy meson suppression at the intermediate p_T. Finally, as we will see immediately, the different path length dependence of induced radiation and collisions energy dissipation makes the latter an indispensable component in the analysis of small collision systems.

We take the collisional energy loss obtained in hard-thermal loop (HTL) calculations [7]. The energy loss of a quark per unit length in a weakly coupled thermal plasma is given by

$$\frac{dE_{\rm el}}{d\Delta z} = \frac{C_F}{4}\left(1+\frac{N_f}{6}\right)\alpha_s(ET)g_s^2T^2 \times \ln\left(\frac{ET}{m_D^2}\right)\left(\frac{1}{v}-\frac{1-v^2}{2v^2}\ln\frac{1+v}{1-v}\right), \quad (23)$$

with $v = p/E$ being the velocity of the parton in the rest frame of the QGP, applied to both heavy and light quarks. Gluon energy loss is related to that of the quark via the C_A/C_F quadratic Casimir ratio. The running coupling value at one loop is used in the above expression [90], where the maximum α_s is cutoff at $g_s^2/(4\pi)$. We remark that the running coupling effect cancels the $\ln(ET/m_D^2)$ enhancement from phase-space integration and results in an approximately energy-independent collisional energy loss.

In this study, we use averaged collisional energy loss, with hard parton production and Δz integration following the same distributions and trajectories as in obtaining the averaged in-medium splitting functions. We then apply the collisional energy loss to partons created in the hard process before invoking the in-medium splitting function modification of the fragmentation function. The justifications for this approximation are that (1) collisional energy loss is almost E-independent, and (2) a $\Delta E_{\rm el}$ mismatch will only cause a small difference in the QCD evolution so long as $\Delta E_{\rm el} \ll Q$.

C. Medium size dependence of radiative and collisional energy loss

While we employs the full expressions [equations (11) and (12)] in the calculation, it is instructive to look at the radiative parton energy loss obtained in the $x \to 0$ limit. The energy loss fraction $\Delta E/E = \int x\frac{dN_{\rm med}}{dx}dx$ in this approximation is

$$\frac{\Delta E_{\rm rad}}{\alpha_s C_R} = \int d\Delta z \frac{2m_D^2\Delta z}{\lambda_g}\int\frac{du}{u^2}\left[\gamma_E + \ln(u) + \frac{\pi}{2}\sin(u) - \cos(u)\mathrm{Ci}(u) - \sin(u)\mathrm{Si}(u)\right] \quad (24)$$

$$= \int d\Delta z \frac{2m_D^2\Delta z}{\lambda_g}\left[\frac{\pi}{2}\ln\frac{2E}{m_D^2\Delta z} + \cdots\right], \quad (25)$$

with $u = m_D^2\Delta z/2xE$. The second line shows the asymptotic behavior at high energy, where the ellipsis standards for terms not enhanced by $\ln E$. Compared with the scaling of the elastic energy loss fraction

$$\frac{\Delta E_{\rm el}}{\alpha_s C_R} \propto \int m_D^2 d\Delta z, \quad (26)$$

one sees that radiative energy loss rate only dominates over the elastic one by $\alpha_s\Delta z T\ln\frac{2E}{m_D^2\Delta z}$. Furthermore, they scale differently with medium size. For example, in a QGP that undergoes Bjorken expansion such that $T^3\tau = T_0^3\tau_0$ and $\Delta z = \tau - \tau_0$, the typical momentum transfer and the mean-free path evolve with proper time as $m_D^2 = m_{D,0}^2(\tau_0/\tau)^{2/3}$ and $\lambda_g = \lambda_{g,0}(\tau/\tau_0)^{1/3}$. Therefore, neglecting the Δz dependence in the logarithmic factor, the radiative energy loss fraction

$$\Delta E_{\rm rad} \propto \int_{\tau_0}^{\tau_0+L}\frac{2m_D^2}{\lambda_g}\Delta z d\Delta z \propto L \quad (27)$$

only scales linearly with size. At the same time, the elastic energy loss fraction

$$\Delta E_{\rm el} \propto \int_{\tau_0}^{\tau_0+L} m_D^2 d\Delta z \propto L^{1/3} \quad (28)$$

changes much slower with L. Consequently, one expects that collisional processes becomes increasingly important in a small-sized QGP.

D. Modified quantum chromodynamics evolution equations for in-medium fragmentation

To compute hadron production in a nuclear environment, we take the modified DGLAP approach [33,69,91] to evolve the vacuum fragmentation function from an initial nonperturbative scale Q_0 to $Q = p_T + \Delta E_{\rm el}$ with medium modified QCD splitting functions described in Sec. IV A.

a. Evolution in the vacuum. The evolution equation for the fragmentation function $D_{h/i}^0$ of hadron specie h from parton i produced in the vacuum is

$$\frac{\partial D_{h/i}(z,Q^2)}{\partial\ln Q^2} = \sum_j\int_z^1\frac{dx}{x}D_{h/j}\left(\frac{z}{x},Q^2\right) \times[P'_{ji}(x\to 1-x,Q^2) + d_{ji}(Q^2)\delta(1-x)], \quad (29)$$

where $i = q, g$ and H, with H denoting heavy quarks. Note that we adhere to the standard high-energy definition of the momentum fraction x in the DGLAP equation: z is the momentum fraction of the produced hadron relative to the momentum of parton i, x is the momentum fraction retained

by the parent parton i. P'_{ji} are QCD splitting functions as defined in equations (18) but with $x \to 1-x$ as indicated, and correspondingly singularities that go as $1/(1-x)$ are replaced by the plus function $1/[(1-x)_+]$. The running coupling is evaluated at Q^2 for the vacuum evolution. The $d_{ji}\delta(1-x)$ terms are virtual corrections that only appear in the diagonal terms ($d_{gq} = d_{gH} = d_{qg} = d_{Hg} = 0$). The diagonal terms d_{qq}, d_{HH}, and d_{gg} can be determined by imposing the conservation of flavor and light-cone momentum [32]. For $i = q, H$, they are

$$0 = \int_0^1 [P'_{ii}(1-x, Q^2) + d_{ii}\delta(1-x)]dx, \tag{30}$$

which solves to

$$d_{qq}(Q^2) = \frac{\alpha_s(Q^2)}{2\pi} C_F \frac{3}{2}, \tag{31}$$

$$d_{HH}\big(Q^2, r\big) = \frac{\alpha_s(Q^2)}{2\pi} C_F c_{HH}(r). \tag{32}$$

The condition for the gluon reads

$$0 = \int_0^1 x[P'_{gg}(1-x, Q^2) + d_{gg}\delta(1-x)]dx + \int_0^1 x \sum_{i=u,d,s,c,b} P'_{ig}(1-x, Q^2)dx, \tag{33}$$

resulting in

$$d_{gg}(Q^2, r) = \frac{\alpha_s(Q^2)}{2\pi}\frac{11}{6}N_c + \frac{\alpha_s(Q^2)}{2\pi} T_F \left[\sum_{H=c,b} c_{gH}(r) - \frac{2}{3}N_f\right]. \tag{34}$$

If allowed by kinematics, d_{gg} and d_{HH} can depend on the ratio $r = M/Q$ with

$$c_{gH}(r) = F\left(\frac{1+\sqrt{1-4r^2}}{2}\right) - F\left(\frac{1-\sqrt{1-4r^2}}{2}\right) - 2r^2\sqrt{1-4r^2}, \tag{35}$$

$$F(x) = -x^4 + \frac{4}{3}x^3 - x^2, \tag{36}$$

$$c_{HH}(r) = \frac{(1+2r^2)(3+2r^2)}{2(1+r^2)^2} - 2\ln\frac{1}{1+r^2}. \tag{37}$$

Finally, the relation between Q^2 and $x, \mathbf{k}$ and the allowed kinematic ranges are summarized in Table I for each channel.

b. Evolution in the medium. For the QCD evolution in the medium, the splitting functions and virtual corrections in equation (29) are replaced by the medium-modified ones,

$$P'_{ji} \to P'_{ji} + \mathbf{k}^2 \frac{dN^{\text{med}\prime}_{ji}}{dxd\mathbf{k}^2}, \quad \text{with } x \to 1-x, \tag{38}$$

and

$$d_{ji}\big(Q^2\big) \to d_{ji}(Q^2) + d^{\text{med}}_{ji}(Q^2). \tag{39}$$

$dN^{\text{med}\prime}_{ji}$ can be obtained from equations (11) and (12) with the substitution $x \to 1-x$. The $1/(1-x)$ terms are then factored out where applicable and supplemented by the "plus"-function prescription. d^{med}_{qq}, d^{med}_{HH}, and d^{med}_{gg} are similarly obtained by imposing flavor and light-cone-momentum conservation for the medium corrections,

$$0 = \int_0^1 \left[\mathbf{k}^2 \frac{dN^{\text{med}\prime}_{qq}}{dxd\mathbf{k}^2} + d^{\text{med}}_{qq}\delta(1-x)\right]dx, \tag{40}$$

$$0 = \int_0^1 \left[\mathbf{k}^2 \frac{dN^{\text{med}\prime}_{HH}}{dxd\mathbf{k}^2} + d^{\text{med}}_{HH}\delta(1-x)\right]dx, \tag{41}$$

$$0 = \int_0^1 x\left[\mathbf{k}^2 \frac{dN^{\text{med}\prime}_{gg}}{dxd\mathbf{k}^2} + d^{\text{med}}_{gg}\delta(1-x)\right]dx + \int_0^1 x \sum_{i=u,d,s,c,b} \mathbf{k}^2 \frac{dN^{\text{med}\prime}_{ig}}{dxd\mathbf{k}^2}dx. \tag{42}$$

The medium-induced correction to the splitting function does not introduce a $\ln Q^2$ dependence as strong as the vacuum one because it decays as $1/\mathbf{k}^4$ or faster at large $\mathbf{k}^2$ and is screened by the Debye mass m_D at small $\mathbf{k}^2$. In the low-Q^2 region, the medium modifications become comparable to or can even dominate over the vacuum contribution. When this happens, one has to consider how to implement such corrections. For example, in Ref. [95], the authors only apply the modified DGLAP equation to the region $Q > 1$ GeV, and use the medium-modified QCD splitting function below 1 GeV to build an in-medium initial condition of the evolution. Other methods treat the low-Q^2 region in a transport approach [96–99] where multiple medium-induced emissions are generated sequentially in a time-ordered fashion because the number of soft emissions is enhanced by the medium size. In our calculation, we notice that with the choice $Q^2 = \mathbf{k}^2/[x(1-x)]$, Q^2 is inversely proportional to the formation time of the branching $\tau_f = p^+/Q^2$. For soft emissions that do not significantly change p^+, the Q^2-ordered evolution is the same as a formation time ordered approach to compute radiative parton energy loss. However, they are not the same for energetic splittings that take a large fraction of the parton energy. We further remark that the QCD evolution approach can be applied to regions where the branching fraction x is large and regions where the medium correction is negative due to interference, which are beyond the scope of the transport equation. This may be important for small collisions systems, as the interference effects are very sensitive to a small path

TABLE I. Q^2 in terms of splitting kinematics and the kinematic ranges of Q^2 (or of x).

Channel	Q^2 definition	Q^2 constraints	x constraints
Light flavors	$\frac{\mathbf{k}^2}{x(1-x)}$	$Q^2 > \Lambda^2_{\text{QCD}}$	
HH	$\frac{\mathbf{k}^2+(1-x)^2M^2}{x(1-x)}$	$Q^2 > \frac{1-x}{x}M^2$	$x > \frac{r^2}{1+r^2}$
gH	$\frac{\mathbf{k}^2+x^2M^2}{x(1-x)}$	$Q^2 > \frac{x}{1-x}M^2$	$x < \frac{1}{1+r^2}$
			$x > \frac{1-\sqrt{1-4r^2}}{2}$
Hg	$\frac{\mathbf{k}^2+M^2}{x(1-x)}$	$Q^2 > \frac{M^2}{x(1-x)} \geqslant 4M^2$	$x < \frac{1+\sqrt{1-4r^2}}{2}$

length. Therefore, we consider the QCD evolution approach to be a better choice for the system-size scan down to small collisions systems such as O-O and p-Pb. In addition, its predictions for light hadron quenching in large systems have been verified by experimental measurements [32,33].

Both the vacuum and in-medium evolution use vacuum fragmentation functions at $Q_0 = 0.4$ GeV as the initial condition. The QCD evolution approach, similar to the traditional energy-loss approach, assumes that hadronization happens outside of the medium. However, for heavy mesons, the formation time can be significantly shortened by the large mass [100,101]. This may have additional phenomenological consequences and we will come back to this point in Sec. VI B.

We take the charged-pion fragmentation functions as extracted from global analysis in Ref. [102]. The fragmentation functions' initial conditions are parametrized at $Q = 1$ GeV, which is comparable to the typical k_T of the medium-modifications. To incorporate all medium contributions, we first use the vacuum DGLAP to evolve these fragmentation functions down to $Q = 0.4$ GeV. They provide the common initial condition for evolution in the vacuum and the medium and we have verified that the vacuum results evolved back to $Q = 1.0$ GeV reproduce the original parametrization. Because the peaking contributions of the medium-induced splitting functions only come into play at perturbative values of k_T (as shown in Fig. 3), so long as we focus on describing R_{AB} at $Q = p_T \gg 1$ GeV, uncertainties introduced from running vacuum DGLAP evolution from $Q_0 = 0.4$ to $Q = 1$ GeV will cancel against the initial condition that is obtained by evolving the fragmentation function from $Q = 1$ down to $Q_0 = 0.4$. The choice of $Q_0 = 0.4$ GeV is merely to be consistent with the nonperturbative cutoff that we introduced when tabulating the medium-induced contribution as given by equations (11) and (12), i.e., $Q = \{\mathbf{k}^2/[x(1-x)]\}^{1/2} > 2k_{T,\min} = 0.4$ GeV.

We use the Lund-Bowler function [103] to parametrize the initial condition at $Q = 0.4$ GeV for the heavy quark fragmenting to a heavy meson (up to a normalization factor),

$$D(z) = z^{-1-bM_\perp^2}(1-z)^a e^{-bM_\perp^2/z}. \tag{43}$$

We have verified that with parameters $a = 0.89$, $b = 3.3$ GeV^{-2}, and $M_\perp^2 \approx M_{c,b}^2 + (0.7\ \text{GeV})^2$,[3] the evolved $D(z, Q)$ provide a reasonable description to heavy-meson fragmentation measurements by the CLEO Collaboration [92] at $Q = M_{\Upsilon(4S)}/2$ and the ALEPH Collaboration [93,94] at $Q = M_Z/2$. In Fig. 4, dashed lines are the Lund-Bowler initial conditions and blue lines are fragmentation functions evolved to $Q = p_T = M_z/2$ for the ALEPH experiment and $Q = p_T = M_{\Upsilon(4S)}/2$ for the CLEO experiment. Blue bands denote variation $p_T/2 < Q < 2p_T$. In this study, we set the initial condition for heavy mesons produced from gluon fragmentation to zero. The DGLAP evolution will generate finite perturbative $g \to D, B$ contributions at higher scale starting from order α_s. However, it is shown in a global fit [105]

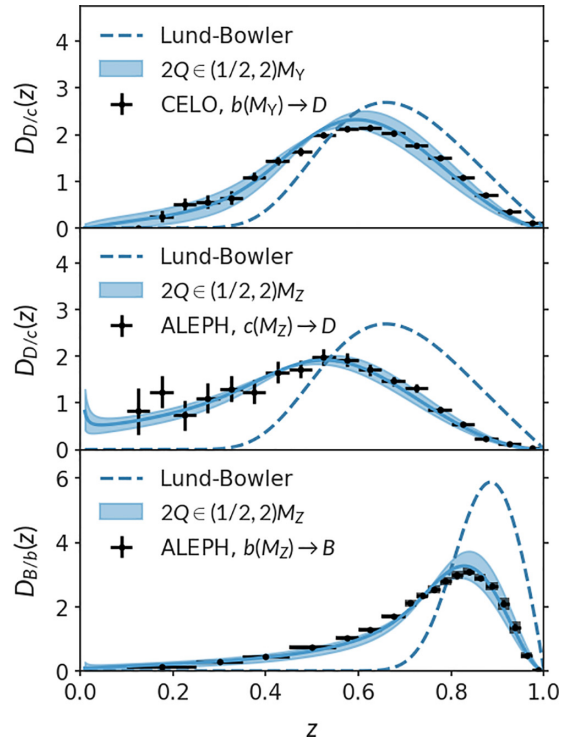

FIG. 4. Heavy-meson fragmentation function evolved from the Lund-Bowler-type initial condition are compared with data. CLEO [92] data on D and D^* fragmentation are obtained at the $\Upsilon(4S)$ threshold ($\approx$10 GeV). The ALEPH [93,94] experiment measures charm and bottom fragmentation functions at $M_z \approx 92$ GeV. The bands correspond to variation of Q by factors of 1/2 and 2. Dashed lines indicate the Lund-Bowler initial conditions for each case.

that nonperturbative $g \to D, B$ fragmentation is small but not negligible, because it is enhanced by the large gluon production cross section in hadronic colliders at high energies. This can have phenomenological impact when we simultaneously study the nuclear modification factors of light and heavy flavors as we will comment in Sec. VI B.

In Fig. 5, we compare the fragmentation functions in p-p (blue solid lines) and in 0%–5% central Pb-Pb collisions (red dashed lines and bands) for six different fragmentation processes evolved from $Q = Q_0$ to $Q = p_T = 50$ GeV. The blue solid lines are the evolved results in the vacuum, and the red dashed lines with bands are results evolved in the medium with $g_s = 1.6, 1.8, 2.0$. Compared with $D(z)$ in the vacuum, medium-modified DGLAP evolution "redshifts" $D(z)$. In the calculation of inclusive hadron spectra, $D(z)$ is always folded with a steeply falling partonic cross section. Thus, the spectra of both heavy and light hadrons are mostly sensitive to the behavior and modifications of $D(z)$ near $z = 1$, even though the pion fragmentation functions (the top row) are much softer than those of heavy mesons (middle and bottom rows).

V. DYNAMICAL SIMULATIONS OF QUARK GLUON PLASMA AND ITS EXISTENCE IN SMALL SYSTEMS

Finally, we discuss the model for the medium evolution. The dynamical simulation of the quark-gluon plasma

[3]These values of a and b parameters are close to but slightly different from those used in Ref. [104].

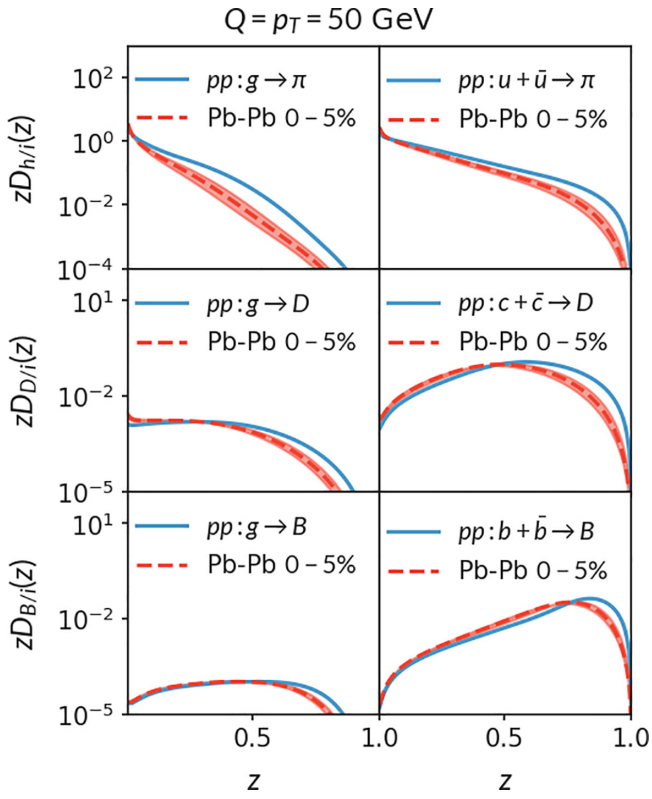

FIG. 5. Modified fragmentation functions in 0%–5% Pb-Pb collisions at 5.02 TeV. From left to right, top to bottom panels are for $g \to \pi$, $u + \bar{u} \to \pi$, $g \to D$, $c + \bar{c} \to D$, $g \to B$, $b + \bar{b} \to B$, respectively. The blue solid lines are the evolved ($Q = p_T = 50$ GeV) fragmentation functions in the vacuum for proton-proton collisions. Red dashed lines with bands are results in 0%–5% central Pb-Pb collisions, varying $g_s = 1.8 \pm 0.2$.

produced in nuclear collisions is performed using the Duke HIC-EVENTGEN code package [106]. In this calculation, the TRENTo initial condition model of the collision geometry provides the energy deposition profiles at the proper time $\tau = 0^+$. The model of quark-gluon plasma dynamics consists of a pre-equilibrium stage modeled by free-streaming [107], followed by the $2 + 1$D boost-invariant relativistic viscous hydrodynamics [108,109]. Finally, the hydrodynamic fields are particlized into hadrons at transition temperate $T_{\rm sw}$ slightly below the pseudocritical temperature of the QGP equation of state [110], and the hadronic interactions are handled by the ultrarelativistic-quantum-molecular-dynamics (UrQMD) code [111,112]. The model parameters have been tuned to the experimental measurement of particle production, flows, and correlations in previous studies [106].

In the current study, it will be very computationally intensive to obtain the full splitting functions and perform DGLAP evolution on an event-by-event basis. Therefore, we simulate events with centrality-averaged initial conditions. For this reason, the scale parameter (normalization) of the TRENTo energy deposition model is retuned for each system to reproduce the centrality-dependent charged particle yield and transverse energy. Because no data are available for nuclear collisions at 7 TeV, we interpolate the normalization tuned at RHIC and LHC energies using a third-degree polynomial in $\ln \sqrt{s}$ to predict the normalization for O-O collisions at 7 TeV. The details can be found in Appendix A.

Now, we discuss the existence of QGP effects in small systems. This may naively seem to be an unnecessary discussion, because the hydrodynamic simulations already provide the time evolution of the temperature profile. One can, in principle, use this to compare the medium temperature and the QGP pseudocritical temperature T_c to determine if the jet propagates in the QGP phase or in a hadronic phase. In fact, for those high-multiplicity events in small system collisions, the simulated medium temperature starts from a point well above T_c (see Appendix A). However, the definition of temperature in the hydrodynamics-based simulation bears certain ambiguity when the system is far from equilibrium, for example, in small colliding systems. On the other hand, in the hydrodynamic picture if it is indeed valid, energy density is converted into temperature using the lattice QCD EoS, which means that the number of scattering centers defined in this manner would approach the thermal limit. If the system is far from equilibrium, the density of scattering centers can significantly deviate from this expectation. In this study, we will therefore investigate two extreme limits of small colliding systems:

(i) calculations with cold nuclear matter effect only;
(ii) calculations with cold and hot medium effects that assume the QGP is described by the hydrodynamic model.

We let future experiments falsify either scenario.

VI. RESULTS AND DISCUSSION

In the result section, we first illustrate the type of modification cold nuclear matter effect and QGP effects may induce in the cross-section ratio R_{AA}. Next, a range for the jet-medium coupling parameter g_s in large colliding systems Au-Au, Pb-Pb, and Xe-Xe is fixed. With the same set of parameters, we then present predictions for R^h_{AA}, R^D_{AA}, and R^B_{AA} in d-Au, p-Pb, and O-O collisions. These calculations are performed with the dynamical cold nuclear matter effects. We discuss the impact of using the dynamical approach and the nuclear PDF in Appendix C. We also compare our baseline calculations in proton-proton collisions with experimental data in Appendix B.

A. Interplay of cold (initial-state) and hot (final-state) medium effects

In Fig. 6, we sequentially include the contribution from Cronin effect and coherent power corrections, CNM energy loss, elastic and radiative effect in the QGP in central Pb-Pb, p-Pb and O-O collisions (columns). The coupling between the partons and the medium used in this demonstration is $g_s = 1.8$. Rows from top to bottom show the modifications for charged hadrons, D mesons, and B mesons. The dotted lines include only Cronin momentum broadening and the peak for light hadrons is around 3 GeV. For heavier mesons, it moves to slightly higher p_T. The inclusion of CNM energy loss (black

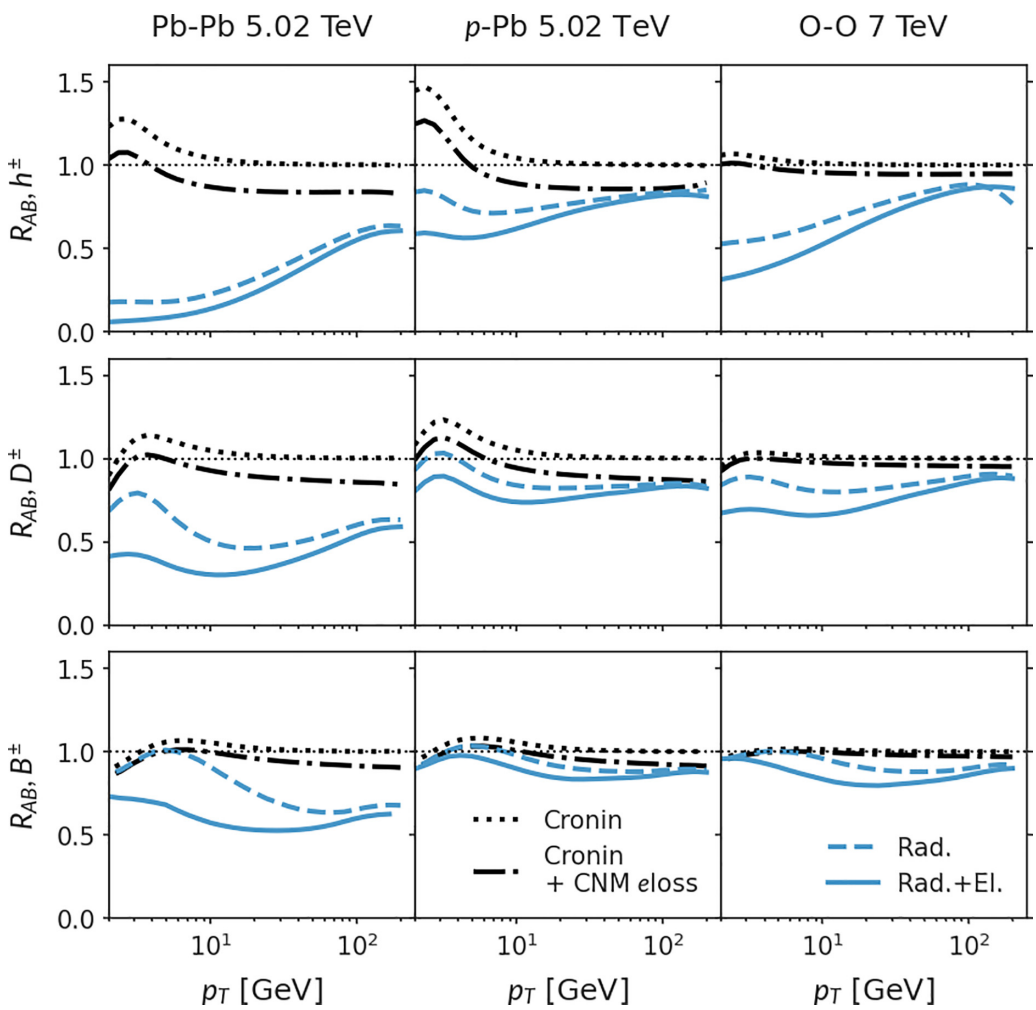

FIG. 6. Nuclear modification factor R_{AB} of light hadron (left column), charm (center column) and bottom (right column) mesons in 0%–10% central Pb + Pb collisions at 5.02 TeV (top row), 0%–1% high-multiplicity p-Pb collisions at 5.02 TeV (middle row), and 0%–10% central O + O collisions at 7 TeV (bottom row). Within each panel, we show R_{AB} results that sequentially include the Cronin and dynamical shadowing effects (black dotted lines), CNM energy loss (black dash-dotted lines), medium-induced radiation (blue dashed lines), and collisional energy loss (all effects, blue solid lines).

dash-dotted lines) results in an overall suppression at high p_T. CNM effects are much smaller in O-O collisions than those in Pb-Pb collisions, as expected from the $A^{1/3}$ scaling.

In Pb-Pb collisions, the modified QCD splitting functions (calculations shown as blue dashed lines) lead to significant suppression of light hadron production. The further inclusion of collisional energy loss (solid blue lines) is a subleading effect in $\ln(E)$. For heavy mesons, the radiative correction in the region $p_T < 5M$ is strongly suppressed, and the modifications are largely attributed to collisions energy loss. One should be careful, however, when interpreting the heavy-flavor results at $p_T \lesssim M$. In this region, the "jet approximation" $E \gg M$ completely breaks down, and the heavy quark's orientation can change randomly as it "diffuses" in the QGP. The low-p_T regime is better modeled by Langevin or other transport approaches that fully evolve the phase-space density of the heavy quark [113–115]. In central p-Pb and O-O collisions, there is a notable change in the relative importance of radiative correction and collisional energy loss. This can be understood from the different medium-size scaling of the two processes as discussed in Sec. IV C. For heavy mesons in small systems, collisional processes are responsible for at least 50% of the QGP modifications.

B. Nuclear modifications in Pb-Pb, Xe-Xe, and Au-Au

For simplicity of the uncertainty estimation we vary the jet-medium coupling $g_s = 1.8 \pm 0.2$. In principle, g_s may run with the medium scale and this has been investigated in other studies [99]. In Fig. 7, calculations with bands that show the sensitivity to the interaction strength are given for R^h_{AA} (top row), R^D_{AA} (middle row), and R^B_{AA} (bottom row) in Pb-Pb collisions at 5.02 TeV (left column), Xe-Xe collisions at 5.44 TeV (middle column), and Au-Au collisions at 200 GeV (right column). We include the Cronin effect, cold nuclear matter energy loss, and coherent power corrections. Within each panel, the nuclear modification in 0%–10% and 30%–50% central collisions are shown and compared

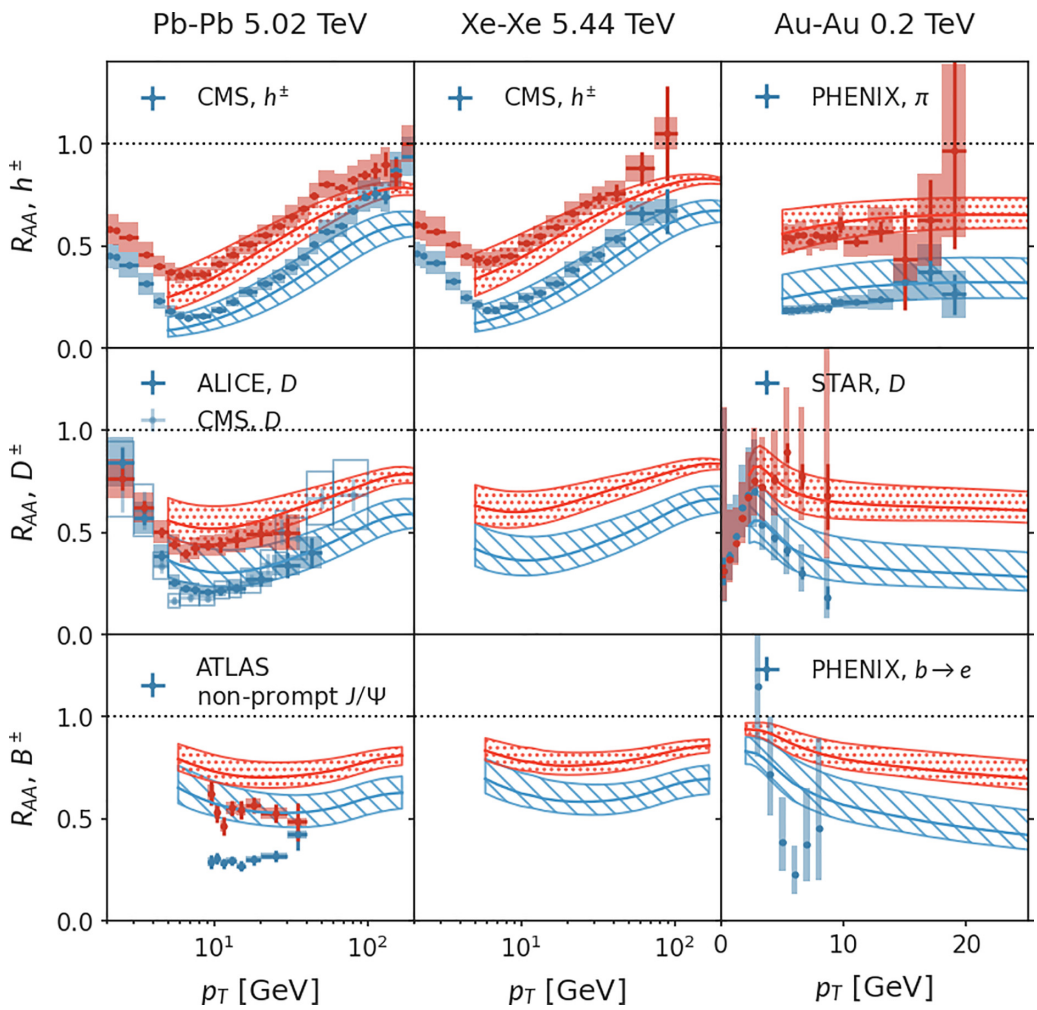

FIG. 7. From top to bottom rows: nuclear modification factor R_{AA} of light hadron, charm and bottom mesons or their decay products in large colliding systems. From left to right columns: Pb + Pb collisions at $\sqrt{s} = 5.02$ TeV for centrality classes 0%–10% and 30%–50%, Xe + Xe collisions at $\sqrt{s} = 5.44$ TeV for centrality classes 0%–10% and 30%–50%, and Au + Au collisions at $\sqrt{s} = 200$ GeV for centrality classes 0%–10% and 40%–50%. The calculations are compared with measurements by the ALICE [116], ATLAS [117], CMS [53,118], PHENIX [119,120], and STAR [121] experiments. For bottom flavor, the B-decayed J/Ψ is computed for the LHC energies and B-decayed electron is presented at RHIC energy. Note that the centrality classes for the STAR measurements of D meson is 0%–10% and 40%–80%.

with available data from the ALICE [116], ATLAS [117], CMS [53,118], PHENIX [119,120], and STAR Collaborations [121] (0%–10% and 40%–80% for STAR D-meson R_{AA}). For comparisons to b-decay electrons and nonprompt J/Ψ, smearing functions extracted from Pythia8 [122] simulations are applied to the B meson spectra.

For light hadron suppression, the range $1.6 < g_s < 1.8$ provides a good description of the LHC data in Pb-Pb and Xe-Xe collisions. At RHIC energy the data suggests a larger coupling $1.8 < g_s < 2.0$. This trend is consistent with many other findings that jet-medium interactions are stronger at lower temperatures relevant for collisions at the RHIC beam energy [36,123]. Our calculations for light mesons using modified fragmentation are only shown for $p_T > 5$ GeV, below which other mechanisms such as hard-soft parton recombination become important [124].

Switching to the flavor or mass dependence of the suppression, the calculation agrees well with D-meson suppression at high transverse momentum but slightly overestimates R_{AA}^D at low p_T. Data tend to lie on the lower edge of the band. The overestimation (not enough suppression) is evident for the bottom quarks. However, we are not going to tune a separate set of parameters for the heavy sector in this paper. Instead, tension with data is a useful indicator of physics that might be missing in the calculation. One improvement we can consider is the use of nonperturbative input to $g \to D, B$ fragmentation at $Q = Q_0$, which then enhances gluon contributions at all Q scales [105]. Because the energy loss of the gluon is a factor of C_A/C_F larger than the quark, an enhanced gluon contribution brings down the inclusive heavy-meson R_{AA}. Another possible explanation for the systematic deviation at low p_T with increasing quark mass is the collisional dissociation of heavy mesons in the QGP [100,125]. In Sec. IV D, we argue that after the evolution the light parton fragmentation should take place outside of the QGP medium. However, the formation time of low-p_T heavy mesons is considerably shorter so that they can be produced inside the nuclear medium. The calculation in Ref. [100] evaluated the collisional broadening and

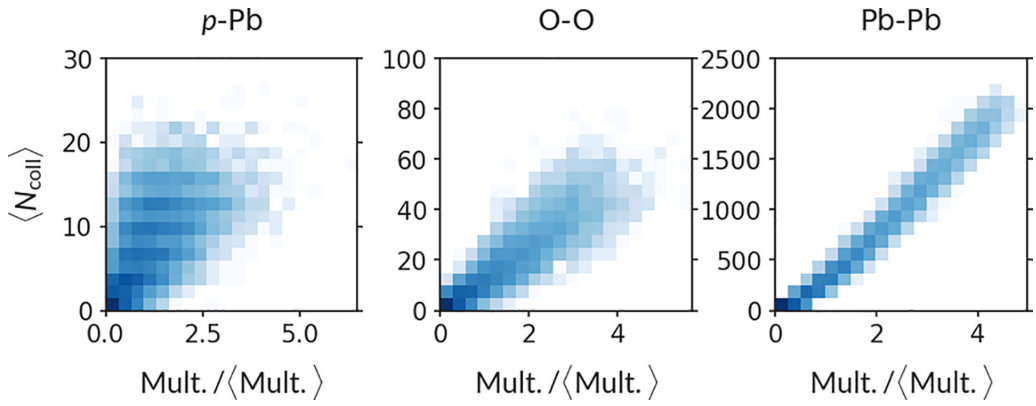

FIG. 8. Correlation between TRENTo centrality classes and the averaged number of binary collisions for p-Pb, O-O, and Pb-Pb collisions. The O-O collisions are expected to establish a more well-defined centrality selection in small collision systems.

break-up of the D and B in the QGP that further suppresses R_{AA}^{D} below 10 GeV and R_{AA}^{B} below 30 GeV. This effect is not included in the present study. However, it should be much less important for calculations in small colliding systems to be discussed in Sec. VI C. Other works consider collisions between D and π, ρ mesons in the hadronic phase [126,127], which is important in the low-p_T region. In addition, Ref. [128] studied M/E-type drag-induced radiations of heavy quarks. These two additional effects qualitatively push the calculation in the right direction, but their overall magnitudes are too small to explain the large difference that we saw in bottom-flavor R_{AA}.

C. Small systems

With the same range of parameters, we now turn to systematic predictions for small collision systems. At LHC energies there have been extensive measurements of jet production in p-A collisions. However, the interpretation of the results suffers from the ambiguity of the geometric model of nuclear collisions in the presence of large fluctuation. This situation is illustrated in Fig. 8 obtained using the TRENTo initial condition model used in this study. From the left to the right panel, we plot the histograms of the self-normalized "multiplicity" at the initial condition level versus the number of binary collisions ($N_{\rm coll} \equiv T_{AB}\sigma_{pp}^{\rm inel}$) for p-Pb, O-O, and Pb-Pb collisions. In large colliding systems, there is a strong correlation between the nuclear geometry and the final-state multiplicity, and the determination of $N_{\rm coll}$ or T_{AB} that normalizes R_{AA} is less sensitive to subnucleonic modeling and fluctuations. This relation strongly decorrelates in p-Pb collisions, making the determination of T_{AB} extremely sensitive to proton shape, fluctuations, and particle production mechanisms. One of the motivations of O-O program is to partly recover the correlation between collision geometry and the multiplicity to provide unambiguous signatures of nuclear modification in small systems. Alternatively, one may consider self-normalized observables in small systems, such as the modification of photon-hadron correlations studied in Ref. [130], to remove the dependence on $N_{\rm coll}$.

First, we study R_{pA} in p-Pb collisions. In Fig. 9 we compare theoretical predictions with *only CNM effects* to the ATLAS data. In theoretical calculations, we always know

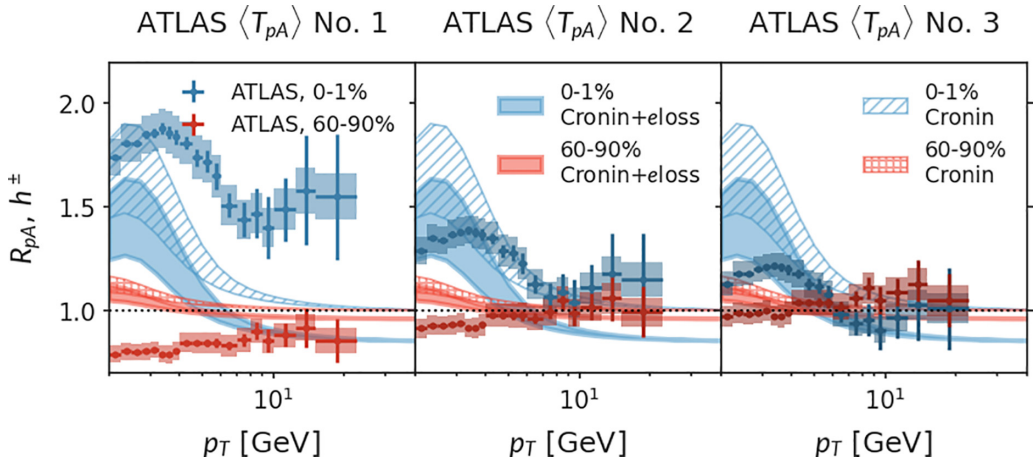

FIG. 9. Nuclear modification factor $R_{p\text{-Pb}}$ compared with ATLAS data [52] scaled by the overlap functions from three different calculations of nuclear collision geometry. The results for 0%–1% and 60%–90% centralities are shown in blue and red, respectively. The calculations only include cold nuclear matter effects. The shaded bands include dynamical shadowing and Cronin effect, while the filled bands further reflect consideration of CNM energy loss.

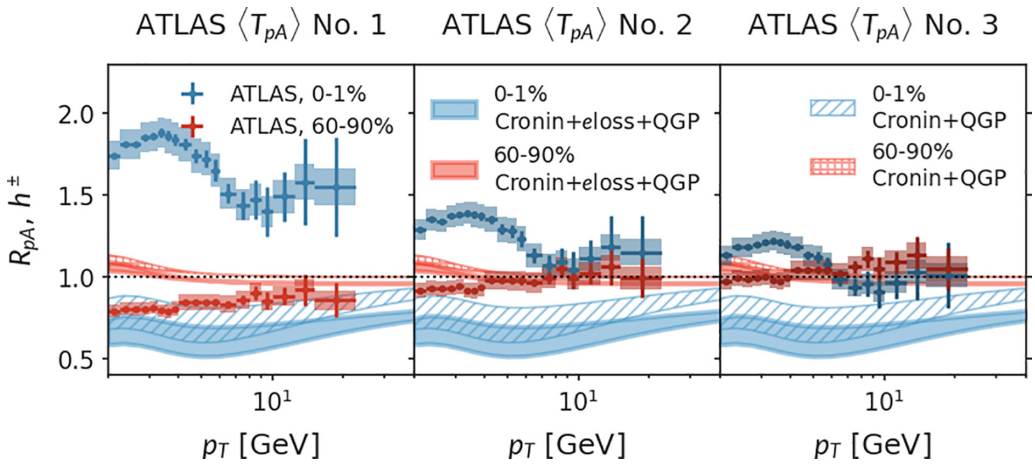

FIG. 10. Same as Fig. 9, but with QGP effect (elastic and radiative) included.

the correct normalization for R_{pA} such that $R_{pA} = 1$ in the absence of nuclear effects. On the experimental side, the published R_{pA} data are strongly model-dependent: the ATLAS Collaboration obtains the normalization $\langle T_{\rm pA}\rangle$ in the conventional Glauber model (left), and the improved Glauber-Gribov model with two choices of a parameter that controls the proton fluctuation (middle and right panels) [52]. Here we label them as ATLAS $\langle T_{\rm pA}\rangle$ #1, #2, and #3. The resulting $Q_{pPb} = dN_{\rm pA\to h}/\langle T_{\rm pA}\rangle/d\sigma_{\rm pp\to h}$ is shown to be extremely sensitive to the experimental choice of the nuclear geometry models.

While the normalization of experimental results are uncertain, we argue that it is unlikely that medium corrections can truly cause 50% enhancement of hadron production at $p_T = 20$ GeV as suggested by geometric model #1. We consider the geometric models #2 and #3 to be much more realistic from the point of view that $R_{AA} \approx 1$ at large p_T. Focusing on scenarios #2 and #3, the cold nuclear matter calculation nicely explains the peak at low p_T in the top 1% high-multiplicity events and its disappearance in 60%–90% p-Pb collisions, although small residual enhancement remains

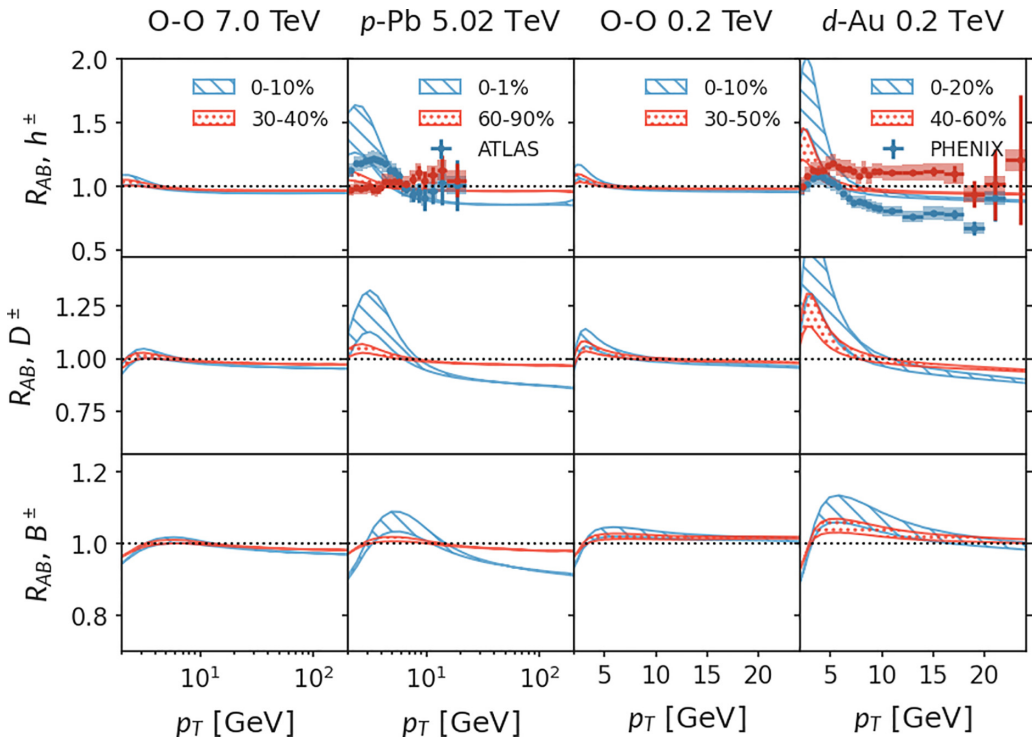

FIG. 11. From top to bottom rows: nuclear modification factor R_{AB} of light hadron, charm, and bottom mesons in small colliding systems. From left to right columns: O-O collisions at $\sqrt{s} = 7$ TeV, p-Pb collisions at $\sqrt{s} = 5.02$ TeV, O-O collisions at $\sqrt{s} = 200$ GeV, and d-Au collisions at $\sqrt{s} = 200$ GeV. The d-Au data is from the PHENIX Collaboration [129]. These calculations only include cold nuclear matter effects.

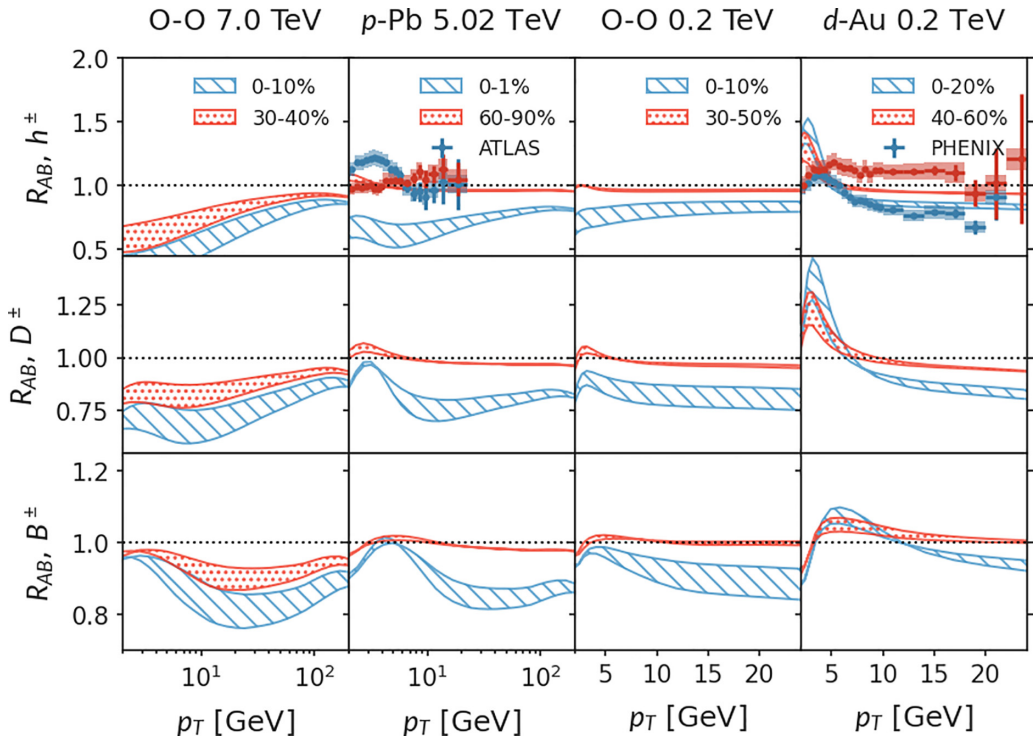

FIG. 12. From top to bottom rows: nuclear modification factor R_{AB} of light hadron, charm, and bottom mesons in small colliding systems. From left to right columns: O-O collisions at $\sqrt{s} = 7$ TeV, p-Pb collisions at $\sqrt{s} = 5.02$ TeV, O-O collisions at $\sqrt{s} = 200$ GeV, and d-Au collisions at $\sqrt{s} = 200$ GeV. The d-Au data is from the PHENIX Collaboration [129]. These calculations include both cold nuclear matter effects and quenching in the QGP.

in peripheral collisions. Also, the peak in the data is at a slightly higher p_T. This "centrality" dependence comes from the nuclear-thickness (impact-parameter) dependence of the Cronin effect. Either calculations with or without CNM energy loss could be consistent with the current data in scenarios #2 and #3, although geometry #2 favors no CNM energy loss. We note that the cold nuclear matter energy loss used here can have an effect at much higher p_T, and modify the production of jets in p-Pb and d-Au, as shown in Ref. [131]. The one used in this paper corresponds to the smaller of the magnitudes that were studied, as it was found to be more compatible with both R_{pA} and R_{CP} measurements. Such modification is further compatible with the suppression of high-p_T hadrons [33] and important to quantitatively describe the suppression of jets at very high p_T [132]. Clearly, a better understanding of nuclear geometry in p-A is needed to further constrain cold nuclear matter effects.

Despite the large model-dependent uncertainty, there is little room left for the hot QGP effects in p-Pb in the current calculation. In Fig. 10, the calculations include both cold and hot nuclear effects. QGP effects introduce a strong centrality dependent suppression of R_{pPb} at intermediate and large p_T. This is not consistent with data in either scenario. However, we would like to emphasize that the temperature of the hot QGP in our simulations is determined by matching the initial condition to hydrodynamic equations using lattice EoS. This cannot exclude models of large nonequilibrium corrections to the density of collision centers in small systems. The initial time for parton-medium interactions $\tau_0 = 0.6$ fm is taken to be the same for large to small colliding systems. It is possible for a medium of lower density created in smaller colliding systems to have a longer hydrodynamization times.

Finally, we present our predictions for O-O collisions. In Fig. 11 we show calculations *with only cold nuclear matter effect* for O-O, p-Pb at the LHC energy and O-O, d-Au at the RHIC energy. Results including hot QGP effects are shown in Fig. 12. Both Figs. 11 and 12 are our predictions in small systems with the current understanding of CNM and QGP effects. If there is no QGP formed in small systems, the CNM effects are small in O-O collisions at both colliding energies. This is contrary to asymmetric collisions like p-Pb and d-Au, where the magnitude of CNM effects depends on the transport properties of cold nuclear matter and phenomenology can only be improved with a better understanding of centrality in $p(d)$-A. This further establishes that the O-O system is ideal to search for QGP effects. If a QGP is created in O-O collisions at $\sqrt{s} = 7$ TeV, we estimate that hot medium effects can lead to almost 50% suppression of the charged-particle R_{AA} at $p_T = 10$ GeV in 0%–10% centrality class, while bottom mesons can be suppressed by 20% at $p_T = 20$ GeV. At $\sqrt{s} = 200$ GeV, the QGP effect in O-O is predicted to be much weaker from a limited lifetime of the fireball. There is about 20% suppression in charged particle R_{AA} in central collisions and negligible effects for 30%–50% collisions.

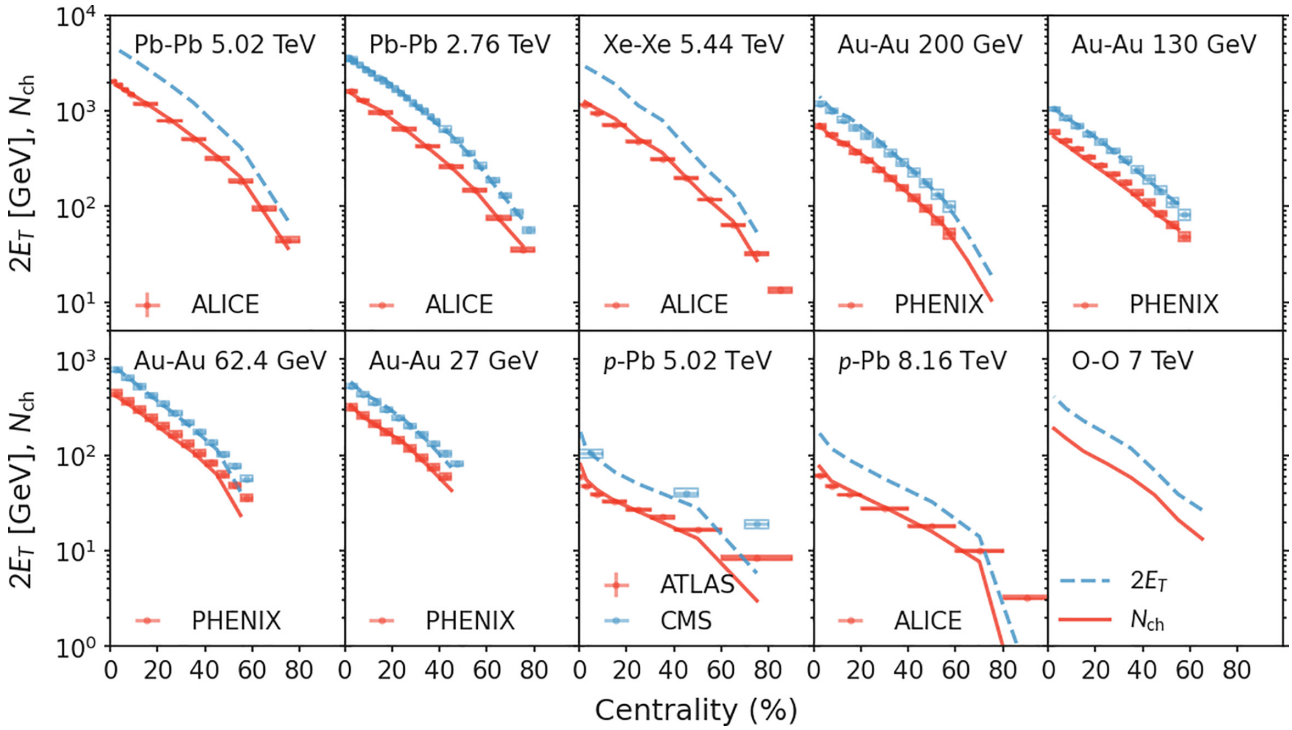

FIG. 13. The multiplicity ($N_{\rm ch}$, red solid lines) and transverse energy (E_T, blue dashed lines) obtained in HIC-EVENTGEN compared with experimental measurements. For symmetric systems, the data at midrapidity are shown. For p-Pb collisions, we take the data within ± 0.5 units of rapidity around the center-of-mass rapidity. The last panel shows the predicted $N_{\rm ch}$ and E_T ($\times 2$) of O-O at 7 TeV using the interpolated TRENTo normalization.

VII. SUMMARY

In this paper, we investigated systematically the modification of light and heavy-flavor hadron production in small and large colliding systems at moderate and high p_T. Our goal was to differentiate the impact of cold nuclear matter and hot QGP effects in the local thermal equilibrium limit. We performed the calculations by including medium-induced corrections into the QCD factorization framework for the more elementary p-p collisions. Cronin effect, coherent power corrections, and parton energy loss in cold nuclear matter modify the initial-state parton densities, while HTL-type collisional energy loss and medium-induced radiative correction change the hadron fragmentation function in the medium. A modified DGLAP evolution approach handles the scale evolution of the fragmentation function in the medium.

With jet-medium coupling $g_s = 1.8 \pm 0.2$, the calculation results in a reasonable agreement with the light flavor suppression in A-A collisions at RHIC and LHC. This range can even accommodate the quenching of charm mesons, albeit with the largest of the studied couplings. However, the same range of g_s underestimates the bottom meson suppression pointing to remaining tensions with the description of bottom quark dynamics even after the inclusion of collisional energy loss.

In small colliding systems we found that the CNM effects alone can already explain the basic patterns observed in p-Pb collisions scaled by the improved Glauber-Gribov model. Room for improvement in the description of such systems is still available, as with the CNM transport parameters used here the magnitude of the Cronin enhancement and/or cold nuclear matter energy loss can be overestimated. One such improvement could be the inclusion of path length fluctuations for initial-state effects. To place tighter constraints on parton transport in large nuclei, a better understanding of centrality determination in p-A reactions will be greatly beneficial. In spite of the remaining uncertainties, we established that the current jet quenching calculation, where we employed a hydrodynamic description of the QGP with formation time $\tau_0 = 0.6$ fm in p-A and locally thermal distribution of quark and gluon quasiparticles, leads to quenching of hadron spectra that is inconsistent with the p-Pb data. This also implies that the contribution from parton energy loss to v_2 in this small asymmetric system cannot be large. The same cannot be said for the d-Au data, where the QGP lifetime is significantly shorter and the measurement leaves room for final-state effects. This once again points to the importance of understanding the centrality determination in highly asymmetric small-on-large systems.

In O-O collisions at RHIC and LHC, we found that CNM effects alone only lead to very small corrections, while the formation of a QGP can suppress charged particle spectra by more than a factor of two at the LHC and by 20% at RHIC energy. Unlike the suppression in large systems that is dominated by induced radiation, collisional energy loss in O-O reactions results in modifications comparable to the effects of in-medium evolution. The predicted suppression in small systems at LHC energies with and without QGP formation is very distinct and can be easily tested with future measurements. We finally observed that if QGP quenching

effects are identified in O-O, the enhanced contribution from collisional processes can be tested by simultaneously looking at the flavor dependence of R_{AA}.

ACKNOWLEDGMENTS

This work is supported by the U.S. Department of Energy, Office of Science, Office of Nuclear Physics through Contract No. 89233218CNA000001 and by the Laboratory Directed Research and Development (LDRD) Program at LANL under project code 20210914PRD2.

APPENDIX A: PARAMETERS FOR HYDRODYNAMIC SIMULATIONS OF O-O COLLISIONS AT 7 TEV

We work in the approximation that the transport parameters are only functions of local temperature and leave them unchanged from those calibrated in Ref. [106]. We assume that only the normalization parameters change notably at different beam energy and fit them using a third-degree polynomial in $\ln\sqrt{s}$. The polynomials are constrained by fitting the normalization to the transverse energy (E_T) production and charged-particle ($N_{\rm ch}$) multiplicity in Au-Au collisions at 27, 62.4, 130, 200 GeV, Pb-Pb collisions at 2.76 and 5.02 TeV, Xe-Xe collisions at 5.44 TeV, and p-Pb collisions at 5.02 and 8.16 TeV. The simulation is performed with centrality-class-averaged initial conditions, and the quality of the description of E_T and $N_{\rm ch}$ at various beam energies is shown in Fig. 13. The polynomial fitting using the extracted normalization factors at different beam energy is shown in Fig. 14, which results in a normalization at 7 TeV to be 19.6. The resulting multiplicity and transverse energy as functions of centrality in O-O is shown in the last panel of Fig. 13. In 0%–10% centrality collisions, $dN_{\rm ch}/d\eta$ is estimated to reach 170. For 30%–40% mid-central collisions, $dN_{\rm ch}/d\eta \approx 58$, which is similar to that in the top 1% high-multiplicity p-Pb collisions.

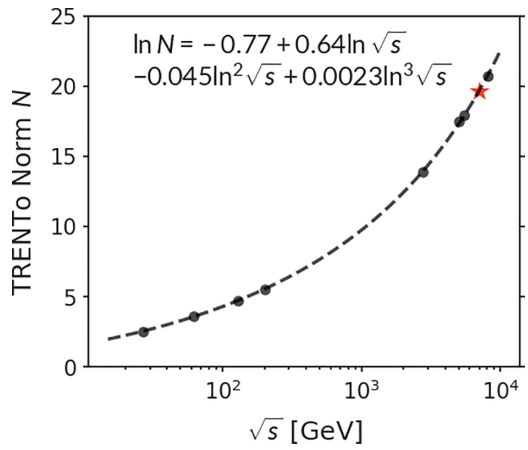

FIG. 14. Normalization parameter of the TRENTo model tuned to Au-Au and Pb-Pb collisions at RHIC and LHC (black circles). Discrete values are fit by $\ln \mathrm{Norm} = a + b\ln\sqrt{s} + c(\ln\sqrt{s})^2 + d(\ln\sqrt{s})^3$ (dashed line) to extrapolate to the normalization parameter at $\sqrt{s} = 7$ TeV (red star).

TABLE II. Maximum temperature reached in hydrodynamic simulations at $\tau = 0.6$ fm.

Systems		$T_{\rm max}$ [GeV]
Pb-Pb 5.02 TeV	0%–10%	0.415
	30%–50%	0.362
Xe-Xe 5.44 TeV	0%–10%	0.401
	30%–50%	0.340
Au-Au 0.2 TeV	0%–10%	0.312
	30%–50%	0.278
p-Pb 5.02 TeV	0%–1%	0.315
	60%–90%	0.174
O-O 7 TeV	0%–10%	0.331
	30%–50%	0.272
d-Au 0.2 TeV	0%–5%	0.225
	40%–60%	0.167
O-O 0.2 TeV	0%–10%	0.237
	30%–50%	0.192

The centrality-dependent temperature profiles from the hydrodynamic simulations are used to obtain the event-averaged medium-modified splitting function, as described in Sec. IV. The jet-medium interactions are turned on from $\tau = 0.6$ fm/c and above $T = 160$ MeV. In Table II, we list the highest initial temperature reached in the hydrodynamic simulations in large and small systems. At the LHC, central p-Pb collisions and O-O collisions starts with maximum initial temperatures $T_{\rm max}$ that are well above the QGP pseudocritical temperature T_c. At the top RHIC energy, $T_{\rm max}$ in central d-Au and O-O collisions are still 70–80 MeV higher than T_c.

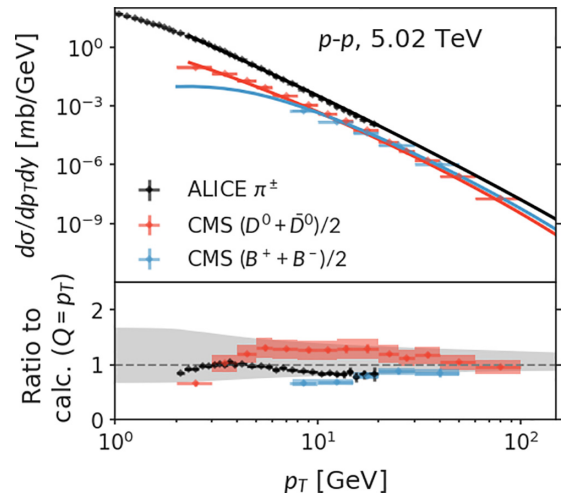

FIG. 15. (upper panel) Comparing calculations in p-p collisions to experimental data, including CMS $D^0(\bar{D}^0)$ meson, $B^{\pm}$ measurements [118,133], and ALICE $\pi^{\pm}$ data [134]. All the experimental data has been converted to the double-differential cross-section $d\sigma/dp_T/dy$. A next-to-leading order K factor 1.4 is used to compare the leading-order results with the data. (lower panel) Ratios of experimental data to calculations with $Q^2 = p_T^2$. The gray band shows the scale variation between $p_T^2/2 < Q^2 < 2p_T^2$ for the calculation of the light hadron.

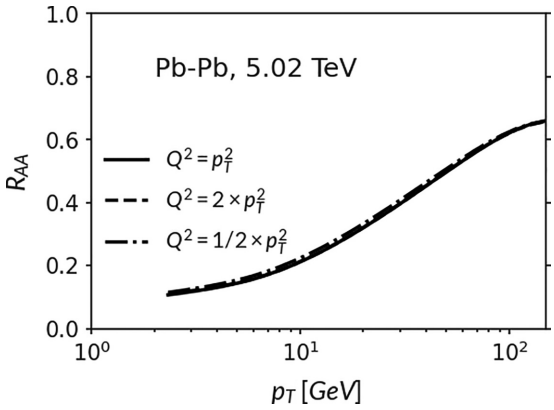

FIG. 16. The scale uncertainty $p_T^2/2 < Q^2 < 2p_T^2$ in the DGLAP (for p-p) and modified DGLAP (for A-B) evolution is largely canceled between particle spectra in nuclear collisions and proton-proton collisions when computing the nuclear modification factor.

APPENDIX B: CROSS SECTION OF LIGHT AND HEAVY MESON PRODUCTIONS IN PROTON-PROTON COLLISIONS

In Fig. 15, we compare our baseline calculation of light and heavy-flavor hadron production in proton-proton collisions to experimental measurements at 5.02 TeV, including CMS data on $h^{\pm}$, D^0, and $B^{\pm}$ [53,118,133] and ALICE measurements of $\pi^{\pm}$ production [134]. All the experimental data have been converted into the double-differential cross-section $d\sigma/dp_T/dy$. We average the cross-section for D and B mesons over its particles and antiparticles but sum over all light hadrons. The perturbative calculation has leading order plus leading-logarithmic accuracy. For the comparisons to D and B meson, the fragmentation fraction $f(c \to D^0) = 0.549$ [135] and $f(b \to B^+) = 0.402$ [136] are used. Note that we have included a next-to-leading order K factor $K = 1.4$ to compare the leading-order plus leading-logarithmic calculations to the data. In general, leading-order calculations have a large-scale uncertainty (the gray band, varying $p_T^2/2 < Q^2 < 2p_T^2$); nevertheless, the shape of the p_T spectra is well reproduced, which is essential for the calculation of R_{AA}. Furthermore, the scale uncertainty coming from the vacuum part of the evolution is largely canceled between the spectra in nuclear collisions and the proton-proton collision when computing the nuclear modification factor. This has been demonstrated in Fig. 16 that R_{AA} almost stays unchanged with the same range of scale variation as the baseline calculations in Fig. 15.

APPENDIX C: DYNAMICAL COLD NUCLEAR MATTER EFFECT VERSUS NUCLEAR PDF APPROACH

We have done most of our analysis using the dynamical approach for the CNM effects. Finally, we discuss how the signal of hot QGP effects will differ if one performs the calculation with nuclear PDF. In Fig. 17, R_{AA} using dynamical CNM approach (blue dotted bands) are compared with nPDF calculation (gray bands) for Pb-Pb and O-O collisions. For light hadrons and charm mesons, the major differences appear at high p_T, since the dynamical approach does not include modifications in the valence region. B-meson displays a surprising sensitivity to the CNM models at low p_T. Again, these differences show up in the region where $M/p_T = O(1)$, which is not a well-controlled region in the current framework. Nevertheless, this difference suggests that when hot medium effects are suppressed by the large mass of b quark, it is possible to be used to probe the details of the CNM calculation.

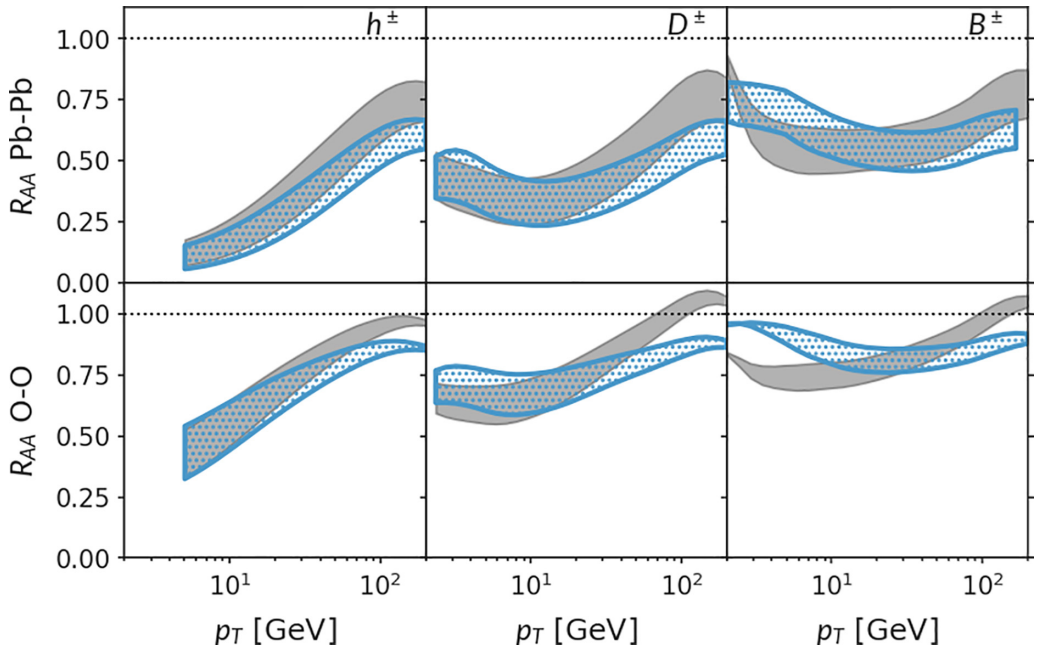

FIG. 17. Impact of different cold nuclear matter effect calculations on the nuclear modification factor in the large and small colliding systems. Blue dotted bands used the dynamical CNM model. The gray bands applied collinear nuclear PDFs from the (n)NNPDF parametrization.

[1] D. A. Appell, Phys. Rev. D: Part. Fields **33**, 717 (1986).
[2] M. Gyulassy and M. Plümer, Phys. Lett. B **243**, 432 (1990).
[3] X.-N. Wang and M. Gyulassy, Phys. Rev. Lett. **68**, 1480 (1992).
[4] R. C. Hwa and X.-N. Wang, *Quark-Gluon Plasma 3* (World Scientific, 2004).
[5] G.-Y. Qin and X.-N. Wang, Int. J. Mod. Phys. E **24**, 1530014 (2015).
[6] M. H. Thoma, Phys. Lett. B **273**, 128 (1991).
[7] E. Braaten and M. H. Thoma, Phys. Rev. D: Part. Fields **44**, R2625 (1991).
[8] M. G. Mustafa and M. H. Thoma, Acta Phys. Hung. New Ser.: Heavy Ion Phys. **22**, 93 (2005).
[9] M. G. Mustafa, Phys. Rev. C **72**, 014905 (2005).
[10] M. Djordjevic, Phys. Rev. C **74**, 064907 (2006).
[11] X.-N. Wang, Phys. Lett. B **650**, 213 (2007).
[12] B. Schenke, M. Strickland, A. Dumitru, Y. Nara, and C. Greiner, Phys. Rev. C **79**, 034903 (2009).
[13] G.-Y. Qin, J. Ruppert, C. Gale, S. Jeon, G. D. Moore, and M. G. Mustafa, Phys. Rev. Lett. **100**, 072301 (2008).
[14] H. Liu, K. Rajagopal, and U. A. Wiedemann, Phys. Rev. Lett. **97**, 182301 (2006).
[15] R. B. Neufeld and I. Vitev, Phys. Rev. C **86**, 024905 (2012).
[16] R. B. Neufeld, I. Vitev, and H. Xing, Phys. Rev. D **89**, 096003 (2014).
[17] R. Baier, Y. Dokshitzer, A. Mueller, S. Peigné, and D. Schiff, Nucl. Phys. B **484**, 265 (1997).
[18] B. Zakharov, JETP Lett. **63**, 952 (1996).
[19] B. Zakharov, JETP Lett. **65**, 615 (1997).
[20] R. Baier, Y. L. Dokshitzer, A. H. Mueller, and D. Schiff, Nucl. Phys. B **531**, 403 (1998).
[21] U. A. Wiedemann, Nucl. Phys. B **588**, 303 (2000).
[22] M. Gyulassy, P. Levai, and I. Vitev, Phys. Rev. Lett. **85**, 5535 (2000).
[23] M. Gyulassy, P. Levai, and I. Vitev, Nucl. Phys. B **594**, 371 (2001).
[24] E. Wang and X.-N. Wang, Phys. Rev. Lett. **89**, 162301 (2002).
[25] P. B. Arnold, G. D. Moore, and L. G. Yaffe, J. High Energy Phys. 06 (2002) 030.
[26] A. Idilbi and A. Majumder, Phys. Rev. D **80**, 054022 (2009).
[27] G. Ovanesyan and I. Vitev, J. High Energy Phys. 06 (2011) 080.
[28] Z.-B. Kang, F. Ringer, and I. Vitev, J. High Energy Phys. 03 (2017) 146.
[29] Y. Makris and I. Vitev, J. High Energy Phys. 10 (2019) 111.
[30] G. Ovanesyan and I. Vitev, Phys. Lett. B **706**, 371 (2012).
[31] M. Fickinger, G. Ovanesyan, and I. Vitev, J. High Energy Phys. 07 (2013) 059.
[32] Z.-B. Kang, R. Lashof-Regas, G. Ovanesyan, P. Saad, and I. Vitev, Phys. Rev. Lett. **114**, 092002 (2015).
[33] Y.-T. Chien, A. Emerman, Z.-B. Kang, G. Ovanesyan, and I. Vitev, Phys. Rev. D **93**, 074030 (2016).
[34] S. Cao and A. Majumder, Phys. Rev. C **101**, 024903 (2020).
[35] S. A. Bass, C. Gale, A. Majumder, C. Nonaka, G.-Y. Qin, T. Renk, and J. Ruppert, Phys. Rev. C **79**, 024901 (2009).
[36] K. M. Burke, A. Buzzatti, N. Chang, C. Gale, M. Gyulassy, U. Heinz, S. Jeon, A. Majumder, B. Müller, G.-Y. Qin, B. Schenke, C. Shen, X.-N. Wang, J. Xu, C. Young, and H. Zhang (JET Collaboration), Phys. Rev. C **90**, 014909 (2014).
[37] C. Andrés, N. Armesto, M. Luzum, C. A. Salgado, and P. Zurita, Eur. Phys. J. C **76**, 475 (2016).
[38] Y. Xu, J. E. Bernhard, S. A. Bass, M. Nahrgang, and S. Cao, Phys. Rev. C **97**, 014907 (2018).
[39] M. Xie, S.-Y. Wei, G.-Y. Qin, and H.-Z. Zhang, Eur. Phys. J. C **79**, 589 (2019).
[40] Y.-T. Chien and I. Vitev, J. High Energy Phys. 05 (2016) 023.
[41] Z.-B. Kang, F. Ringer, and I. Vitev, J. High Energy Phys. 11 (2016) 155.
[42] Y. Tachibana *et al.* (JETSCAPE Collaborations), PoS **Hard-Probes2018**, 099 (2018).
[43] H. T. Li and I. Vitev, Phys. Lett. B **793**, 259 (2019).
[44] S. Chatrchyan *et al.* (CMS Collaboration), Phys. Lett. B **718**, 795 (2013).
[45] B. Abelev *et al.* (ALICE Collaboration), Phys. Lett. B **719**, 29 (2013).
[46] G. Aad *et al.* (ATLAS Collaboration), Phys. Rev. Lett. **110**, 182302 (2013).
[47] A. Adare *et al.* (PHENIX Collaboration), Phys. Rev. Lett. **114**, 192301 (2015).
[48] L. Adamczyk *et al.* (STAR Collaboration), Phys. Lett. B **747**, 265 (2015).
[49] C. Aidala *et al.* (PHENIX Collaboration), Phys. Rev. C **96**, 064905 (2017).
[50] J. Adams *et al.* (STAR Collaboration), Phys. Lett. B **616**, 8 (2005).
[51] S. S. Adler *et al.* (PHENIX Collaboration), Phys. Rev. C **74**, 024904 (2006).
[52] G. Aad *et al.* (ATLAS Collaboration), Phys. Lett. B **763**, 313 (2016).
[53] V. Khachatryan *et al.* (CMS Collaboration), J. High Energy Phys. 04 (2017) 039.
[54] S. Acharya *et al.* (ALICE Collaboration), Phys. Lett. B **783**, 95 (2018).
[55] S. Acharya *et al.* (ALICE Collaboration), Phys. Lett. B **827**, 136943 (2022).
[56] S. Schlichting and P. Tribedy, Adv. High Energy Phys. **2016**, 8460349 (2016).
[57] M. Mace, V. V. Skokov, P. Tribedy, and R. Venugopalan, Phys. Rev. Lett. **123**, 039901(E) (2019).
[58] B. Schenke, C. Shen, and P. Tribedy, Phys. Lett. B **803**, 135322 (2020).
[59] W. Zhao, Y. Zhou, K. Murase, and H. Song, Eur. Phys. J. C **80**, 846 (2020).
[60] A. Adare *et al.* (PHENIX Collaboration), Phys. Rev. Lett. **115**, 142301 (2015).
[61] C. Aidala *et al.* (PHENIX Collaboration), Nat. Phys. **15**, 214 (2019).
[62] J. Adam *et al.* (STAR Collaboration), Phys. Rev. Lett. **122**, 172301 (2019).
[63] Z. Citron *et al.*, CERN Yellow Rep. Monogr. **7**, 1159 (2019).
[64] J. Brewer, A. Mazeliauskas, and W. van der Schee, arXiv:2103.01939 [hep-ph].
[65] Y.-F. Liu, W.-J. Xing, X.-Y. Wu, G.-Y. Qin, S. Cao, and H. Xing, Phys. Rev. C **105**, 044904 (2022).
[66] R. Katz, C. A. G. Prado, J. Noronha-Hostler, and A. A. P. Suaide, Phys. Rev. C **102**, 041901(R) (2020).
[67] A. Huss, A. Kurkela, A. Mazeliauskas, R. Paatelainen, W. van der Schee, and U. A. Wiedemann, Phys. Rev. C **103**, 054903 (2021).
[68] B. G. Zakharov, J. High Energy Phys. 09 (2021) 087.

[69] H. T. Li, Z. L. Liu, and I. Vitev, Phys. Lett. B **816**, 136261 (2021).
[70] M. Gyulassy, I. Vitev, X.-N. Wang, and B.-W. Zhang, Quark –Gluon Plasma **3**, 123 (2004).
[71] S. Chatrchyan *et al.* (CMS Collaboration), Eur. Phys. J. C **72**, 1945 (2012).
[72] M. Gyulassy, I. Vitev, and X. N. Wang, Phys. Rev. Lett. **86**, 2537 (2001).
[73] M. Gyulassy, P. Levai, I. Vitev, and T. S. Biro, Phys. Rev. D **90**, 054025 (2014).
[74] I. Vitev, S. Wicks, and B.-W. Zhang, J. High Energy Phys. 11 (2008) 093.
[75] J.-w. Qiu and I. Vitev, Phys. Lett. B **570**, 161 (2003).
[76] J. W. Cronin, H. J. Frisch, M. J. Shochet, J. P. Boymond, R. Mermod, P. A. Piroue, and R. L. Sumner, Phys. Rev. D: Part. Fields **11**, 3105 (1975).
[77] I. Vitev, Phys. Rev. C **75**, 064906 (2007).
[78] J.-w. Qiu and I. Vitev, Phys. Lett. B **632**, 507 (2006).
[79] I. Vitev, Phys. Lett. B **562**, 36 (2003).
[80] J.-w. Qiu and I. Vitev, Phys. Rev. Lett. **93**, 262301 (2004).
[81] R. B. Neufeld, I. Vitev, and B.-W. Zhang, Phys. Lett. B **704**, 590 (2011).
[82] J. S. Moreland, J. E. Bernhard, and S. A. Bass, Phys. Rev. C **92**, 011901(R) (2015).
[83] M. Gyulassy, P. Levai, and I. Vitev, Phys. Lett. B **538**, 282 (2002).
[84] R. A. Khalek, R. Gauld, T. Giani, E. R. Nocera, T. R. Rabemananjara, and J. Rojo, arXiv:2201.12363.
[85] C. W. Bauer, S. Fleming, D. Pirjol, and I. W. Stewart, Phys. Rev. D: Part. Fields **63**, 114020 (2001).
[86] M. Beneke, A. P. Chapovsky, M. Diehl, and T. Feldmann, Nucl. Phys. B **643**, 431 (2002).
[87] F. D'Eramo, H. Liu, and K. Rajagopal, Phys. Rev. D **84**, 065015 (2011).
[88] G. Ovanesyan, F. Ringer, and I. Vitev, Phys. Lett. B **760**, 706 (2016).
[89] M. D. Sievert, I. Vitev, and B. Yoon, Phys. Lett. B **795**, 502 (2019).
[90] S. Peigné and A. Peshier, Phys. Rev. D **77**, 114017 (2008).
[91] W.-T. Deng and X.-N. Wang, Phys. Rev. C **81**, 024902 (2010).
[92] M. Artuso *et al.* (CLEO Collaboration), Phys. Rev. D **70**, 112001 (2004).
[93] R. Barate *et al.* (ALEPH Collaboration), Eur. Phys. J. C **16**, 597 (2000).
[94] A. Heister *et al.* (ALEPH Collaboration), Phys. Lett. B **512**, 30 (2001).
[95] N.-B. Chang, W.-T. Deng, and X.-N. Wang, Phys. Rev. C **89**, 034911 (2014).
[96] J.-P. Blaizot, F. Dominguez, E. Iancu, and Y. Mehtar-Tani, J. High Energy Phys. 06 (2014) 075.
[97] S. Cao, T. Luo, G.-Y. Qin, and X.-N. Wang, Phys. Rev. C **94**, 014909 (2016).
[98] J. Putschke *et al.*, arXiv:1903.07706.
[99] W. Ke and X.-N. Wang, J. High Energy Phys. 05 (2021) 041.
[100] A. Adil and I. Vitev, Phys. Lett. B **649**, 139 (2007).
[101] C. Markert, R. Bellwied, and I. Vitev, Phys. Lett. B **669**, 92 (2008).
[102] D. de Florian, R. Sassot, M. Epele, R. J. Hernández-Pinto, and M. Stratmann, Phys. Rev. D **91**, 014035 (2015).
[103] M. G. Bowler, Z. Phys. C: Part. Fields **11**, 169 (1981).
[104] J. Abdallah *et al.* (DELPHI Collaboration), Eur. Phys. J. C **71**, 1557 (2011).
[105] D. P. Anderle, T. Kaufmann, M. Stratmann, F. Ringer, and I. Vitev, Phys. Rev. D **96**, 034028 (2017).
[106] J. E. Bernhard, Ph.D. thesis, Duke University 2018 (unpublished).
[107] W. Broniowski, W. Florkowski, M. Chojnacki, and A. Kisiel, Phys. Rev. C **80**, 034902 (2009).
[108] H. Song and U. W. Heinz, Phys. Rev. C **77**, 064901 (2008).
[109] C. Shen, Z. Qiu, H. Song, J. Bernhard, S. Bass, and U. Heinz, Comput. Phys. Commun. **199**, 61 (2016).
[110] A. Bazavov, T. Bhattacharya, C. DeTar, H.-T. Ding, S. Gottlieb, R. Gupta, P. Hegde, U. M. Heller, F. Karsch, E. Laermann, L. Levkova, S. Mukherjee, P. Petreczky, C. Schmidt, C. Schroeder, R. A. Soltz, W. Soeldner, R. Sugar, M. Wagner, and P. Vranas (HotQCD Collaboration), Phys. Rev. D **90**, 094503 (2014).
[111] S. A. Bass *et al.*, Prog. Part. Nucl. Phys. **41**, 255 (1998).
[112] M. Bleicher *et al.*, J. Phys. G **25**, 1859 (1999).
[113] R. C. Hwa and X.-N. Wang, *Quark-Gluon Plasma 4* (World Scientific, 2010), https://www.worldscientific.com/doi/pdf/10.1142/7588.
[114] S. Cao, G.-Y. Qin, and S. A. Bass, Phys. Rev. C **88**, 044907 (2013).
[115] W. Ke, Y. Xu, and S. A. Bass, Phys. Rev. C **98**, 064901 (2018).
[116] S. Acharya *et al.* (ALICE Collaboration), J. High Energy Phys. 10 (2018) 174.
[117] M. Aaboud *et al.* (ATLAS Collaboration), Eur. Phys. J. C **78**, 762 (2018).
[118] A. M. Sirunyan *et al.* (CMS Collaboration), Phys. Lett. B **782**, 474 (2018).
[119] A. Adare *et al.* (PHENIX Collaboration), Phys. Rev. C **87**, 034911 (2013).
[120] A. Adare *et al.* (PHENIX Collaboration), Phys. Rev. C **93**, 034904 (2016).
[121] J. Adam *et al.* (STAR Collaboration), Phys. Rev. C **99**, 034908 (2019).
[122] T. Sjöstrand, S. Ask, J. R. Christiansen, R. Corke, N. Desai, P. Ilten, S. Mrenna, S. Prestel, C. O. Rasmussen, and P. Z. Skands, Comput. Phys. Commun. **191**, 159 (2015).
[123] S. Cao, Y. Chen, J. Coleman, J. Mulligan, P. M. Jacobs, R. A. Soltz, A. Angerami, R. Arora, S. A. Bass, L. Cunqueiro, T. Dai, L. Du, R. Ehlers, H. Elfner, D. Everett, W. Fan, R. J. Fries, C. Gale, F. Garza, Y. He, and Y. Xu *et al.* (JETSCAPE Collaboration), Phys. Rev. C **104**, 024905 (2021).
[124] W. Zhao, W. Ke, W. Chen, T. Luo, and X.-N. Wang, Phys. Rev. Lett. **128**, 022302 (2022).
[125] R. Sharma, I. Vitev, and B.-W. Zhang, Phys. Rev. C **80**, 054902 (2009).
[126] Z.-w. Lin, T. G. Di, and C. M. Ko, Nucl. Phys. A **689**, 965 (2001).
[127] S. Cao, G.-Y. Qin, and S. A. Bass, Phys. Rev. C **92**, 024907 (2015).
[128] S. Cao, A. Majumder, G.-Y. Qin, and C. Shen, Phys. Lett. B **793**, 433 (2019).
[129] U. A. Acharya *et al.* (PHENIX Collaboration), Phys. Rev. C **105**, 064902 (2022).
[130] M. Xie, X.-N. Wang, and H.-Z. Zhang, Phys. Rev. C **103**, 034911 (2021).
[131] Z.-B. Kang, I. Vitev, and H. Xing, Phys. Rev. C **92**, 054911 (2015).

[132] Z.-B. Kang, F. Ringer, and I. Vitev, Phys. Lett. B **769**, 242 (2017).
[133] A. M. Sirunyan *et al.* (CMS Collaboration), Phys. Rev. Lett. **119**, 152301 (2017).
[134] S. Acharya *et al.* (ALICE Collaboration), Phys. Rev. C **101**, 044907 (2020).
[135] D. E. Groom, M. Aguilar-Benitez, C. Amsler, R. M. Barnett, P. R. Burchat, C. D. Carone, C. Caso, G. Conforto, O. Dahl, M. Doser, S. Eidelman, J. L. Feng, L. Gibbons, M. Goodman, C. Grab, A. Gurtu, K. Hagiwara, K. G. Hayes, J. J. Hernández, K. Hikasa *et al.*, Eur. Phys. J. C **15**, 1 (2000).
[136] C. Patrignani, Chin. Phys. C **40**, 100001 (2016).